



Influence of multiple porous structure evolution on physical–mechanical properties and damage mechanism of sandstone heated continuously/periodically with the identical heating time

Yu Zhao^{1,2} · Can Du^{1,2} · Jing Bi^{1,2} · Jiashen Li^{1,2} · Chaolin Wang^{1,2}

Received: 2 March 2022 / Accepted: 14 November 2022 / Published online: 23 November 2022
© Springer-Verlag GmbH Germany, part of Springer Nature 2022

Abstract

This paper studied the physical–mechanical properties and damage mechanism based on porous structure evolution after continuous/periodic heating with identical 10 h of heating. Nuclear magnetic resonance was used to investigate the pore characteristics and microscopic damage of thermally treated sandstone. This research performed Brazilian tensile strength (BTS) and unconfined compressive strength (UCS) tests. The digital image correlation and acoustic emission (AE) techniques were applied to track the strain evolution and monitor the acoustic signal feature during the UCS loading process. The results suggested that, at 200 °C, the periodical heating–cooling specimens show thermal strengthening after multiple thermal cycles, resulting in higher UCS than the continuously heated specimens. However, the UCS of periodical heating specimens is lower than that of the continuously heating ones at 400 ~ 800 °C. In addition, the BTS and UCS initially increased at 200 ~ 400 °C due to thermal-induced enhancement and then decreased at higher temperatures for the continuously heating–cooling specimens. The evolution of mechanical damage based on AE confirmed that periodic heating promotes cracks more in the same heating time. The periodic treatment stimulates the initiation, propagation, and coalescence of nanopores, but mesopores and macropores play a leading role in the mechanical properties. The porous structure evolution is a dynamic process, and the multiple porosities show different characteristics under different temperatures and thermal conditions. Thermal fatigue increases the uniformity coefficient of pores. Repeated treatment at 200 °C enhances the brittleness of sandstone, while periodic heating at high temperatures results in brittle–ductility and failure mode transition.

Keywords Sandstone · Periodic heating · Water cooling · Nuclear magnetic resonance · AE monitoring · Digital image correlation

Introduction

In recent years, with the requested enhancement of geotechnical engineering such as geothermal resources exploitation, deep mining, underground coal gasification, post-fire restoration of underground rock engineering, and deep disposal of high-level radioactive wastes, more and more research has focused on the physical–mechanical properties

of rocks in a high-temperature environment (Kumari et al. 2017; Laouafa et al. 2016). In these environments, sandstone is under continuous or cyclic high temperatures in general, which impairs the long-term stability of the underground engineering rock mass. In underground coal gasification (UCG) projects, the temperature of sandstone overburden can reach about 1000 °C (Laouafa et al. 2016; Niu et al. 2014). Fired underground structures such as tunnels are at a high temperature prior to extinguishing the fire and subjected to quenching during fire extinction. Therefore, the impact of heating–cooling on the physical–mechanical properties of rocks should be considered in the reestablishment after the fire (Ferreira et al. 2014; Smith and Pells 2008). In addition, it is necessary to consider the cyclic water-cooling effect of high-temperature sandstone in the study of cool

✉ Jing Bi
demonjjun@126.com

¹ College of Civil Engineering, Guizhou University, Guiyang 550025, China

² Guizhou Provincial Key Laboratory of Rock and Soil Mechanics and Engineering Safety, Guiyang 550025, China

water recharging in hydrothermal geothermal and water injection in aquifer thermal energy storage (ATES) systems (Fleuchaus et al. 2018; Hähnlein et al. 2013). Therefore, to ensure the safety and sustainable exploitation of underground rock engineering, it is critical to explore further the influence of sandstone microscopic porous structure evolution on macroscopic mechanics under high temperatures.

Numerous studies have shown that high temperatures change physical parameters, impair the pore structure, and weaken the mechanical properties of rocks. The physical properties and strength of sandstone degrade with the temperature rising, which is reflected in the decrease of UCS (Griffiths et al. 2017; Kumari et al. 2017; Ranjith et al. 2012), static splitting strength (Huang et al. 2021; Sirdesai et al. 2016), P-wave velocity, and other physical parameters (Sun et al. 2017a). Some scholars reveal that the BTS and UCS convert from rising to dropping with temperature increase, which may be at 200 °C, 300 °C, 400 °C, and 500 °C, respectively (Chen et al. 2012; Zhao et al. 2022a; Ranjith et al. 2012). The performance enhancement is caused by the closure of micropores/microfractures and free water loss. In terms of deformation analysis, a brittleness-ductility transformation of rock is observed with rising temperatures (23–1100 °C) (Shao et al. 2015; Sirdesai et al. 2017). Besides, some studies have found that the AE signature, such as cracking number and during the time of rocks after or under high temperature, is significantly different from those under normal temperature (Guo et al. 2020; Isaka et al. 2018; Miao et al. 2020; Yu et al. 2020). Many priors have investigated the effect of thermal treatment conditions on the pore structure and permeability characteristics (Meredith et al. 2012; Yavuz et al. 2010). Ding et al. (2016) and Yang et al. (2017) found that the permeability coefficient of sandstone fluctuates slightly in the range of 100–400 °C and the porosity and permeability coefficient increase sharply with a further rise in temperature. Mineral composition and distribution, crack initiation and propagation, and moisture release are the main factors that determine the microstructure and mechanical behavior of sandstone after heating (Bi et al. 2022; Brotóns et al. 2013; Fredrich and Wong 1986; Kim et al. 2014; Kompanikova et al. 2014; Richter and Simmons 1974; Sun et al. 2017b).

Sandstone is however not persistently in a high-temperature state in many cases. In geothermal extraction, rocks around production and reinjection wells will inevitably cool down with cold water injection. Moreover, within different processes of UCG exploitation, the overburden is in temperature cycles. The cyclic thermal treatment will damage the rock structure and significantly alter the strength, elastic modulus, fracture toughness, and permeability (Griffiths et al. 2018; Kumari et al. 2017; Rawal and Ghassemi 2014). Generally, rock quenching will change mechanical behavior and deformation characteristics and enhance permeability (Bi et al. 2020; Breede et al. 2013; Brotóns et al. 2013; Caulk et al.

2016; Grant 2016; Jin et al. 2019; Sarici 2016; Siratovich et al. 2015; Zhu et al. 2018).

However, previous studies have the following shortcomings: (1) In the thermal environment such as UCG surrounding rock and geothermal reservoir, there are not only areas of repeated heat exchange but also areas that maintain high temperatures for a long time. Earlier papers mostly focused on the degradation of rock physical–mechanical properties with the number of thermal cycles. The differences in porous structure and physical–mechanical properties between continuous and periodic heating–cooling have received little attention in a unified time scale. (2) The effect of thermal fatigue on the porous structure is a dynamic process. The previous literature focuses more on porosity, and the quantitative investigation of multiscale pore evolution is insufficient. (3) Unlike the commonly concerned granite, this paper selects sandstone in underground coal gasification surrounding rock (overburden temperature may be as high as 800 ~ 1300 °C) and geothermal reservoir for research.

Given this, this paper conducted low field nuclear magnetic resonance (LF-NMR) and physicommechanical tests on sandstone continuously heated for 10 h and on sandstone periodically heated for a total of 10 h in five cycles at 200, 400, 600, and 800 °C, respectively. The digital image correlation (DIC) technique tracked the surface deformation of specimens, and the AE signal was also recorded in the UCS tests. The research aims to systematically analyze the influence of sandstone microscopic porous structure evolution on macroscopic mechanics with continuous and periodic heating–cooling treatments in the same heating time. The results will support underground coal gasification and geothermal exploitation and contribute to the structure evaluation, repair, and reinforcement of underground engineering exposed to fire conditions.

Experimental details

Specimen preparation

Specimens were taken from the sandstone bedrock of the interior formations in Jiangsu province, China. The sandstone collected for testing mainly consists of quartz, albit, anorthite, and nacrite. The rock specimens are compact, without fractures and macrocracks. A total of 64 specimens were prepared, half made into Brazilian disks with a diameter of 50 mm and a thickness of 25 mm. The rest 32 specimens were made into 100 mm × 50 mm cylinders for the UCS test. All these were applied according to the International Society of Rock Mechanics (ISRM) criterion.

Periodic heating–cooling treatments

In this study, we compared continuous and periodic thermal loading schemes, with identical total heating times (10 h), at 200, 400, 600, and 800 °C, respectively (Fig. 1). Meanwhile, two cooling methods for air and water cooling were set up for each scheme. The specimens were dried in an air-dried oven at 105 °C for 6 h (Han et al. 2019; Pathiranagei and Gratchev 2021), followed by heated from room temperature (25 °C) to the preset temperature at a linear heating rate of 15 °C/min. For continuous heating and then air cooling scheme, once kept at the target temperature for 10 h, the specimen will naturally cool to room temperature. We marked these specimens at different temperatures as A1-200, A1-400, A1-600, and A1-800. In addition, the water cooling sandstone water will be immediately cooled in the 25 °C oscillating thermostatic water tank after heating, recorded as W1-200 to W1-800. For the periodic thermal loading scheme, the specimens were heated for 2 h and then cooled in two different ways, and this is one single cycle. The whole process of the treatment needs to be repeated five times. The total heating time of specimens marked the periodic heating ones was 10 h, the same as that of the continuous heating ones. In this paper, the name of specimens was marked as:

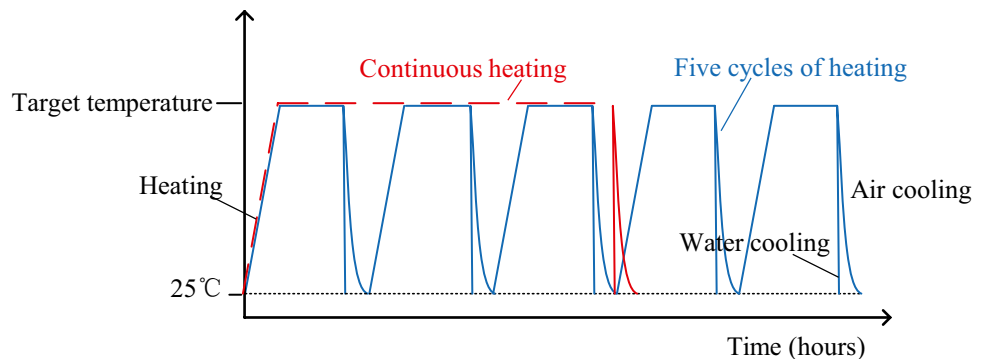
“cooling method (W or A)” + “temperature (200, 400, 600, and 800)” + “-heating scheme (1 represented continuous heating and 2 represented periodic heating)”.

Experimental equipment and methodology

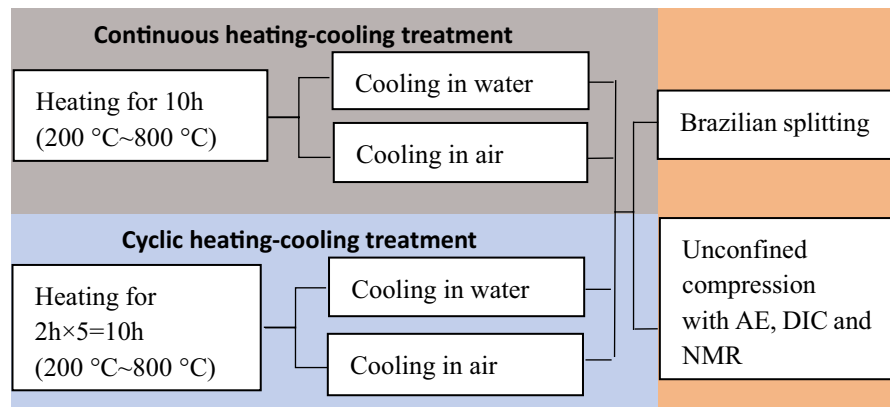
The characteristics and evolution of pore structure were represented by MacroMR-150H-I LF-NMR instrument produced by Suzhou Newmine Analytical Instruments Co. LTD (Fig. 2b). Before measuring, the specimens were vacuumed for 6 h and followed by saturated with distilled water for 24 h. After saturation, we removed the specimens from the water and wiped off the remaining moisture stains on the surface. The samples were wrapped with a cling film to prevent water evaporation caused by the temperature rise during nuclear magnetic resonance.

The DSZ-1000 stress–strain controlled triaxial shear penetration tester was used to carry out the BTS and UCS tests (Fig. 2c). The data acquisition system automatically records all real-time data 5 times per second. The BTS and UCS tests were performed at 0.05 kN/s and 0.05 mm/min loading rates, respectively. Furthermore, we employed DIC to record the evolution of the total strain field on the sandstone surface during uniaxial compression.

Fig. 1 The schematic diagram of the experimental procedure of thermally loaded sandstone

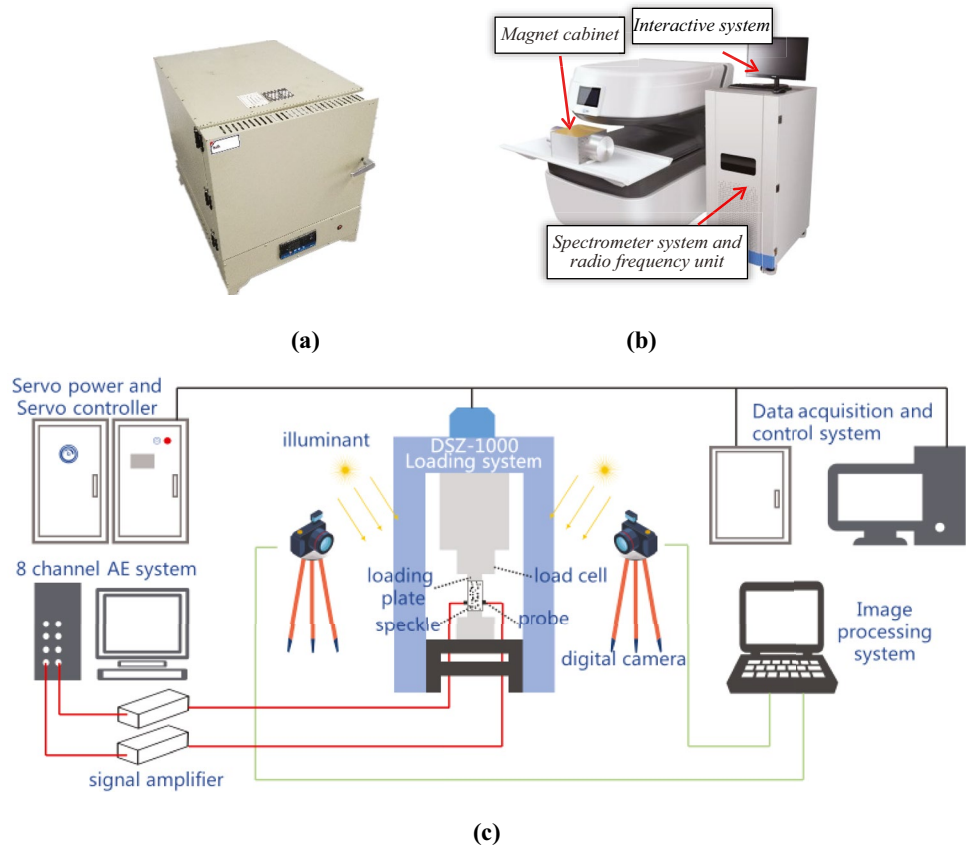


(a) schematic diagram of thermal loading.



(b) complete experiment procedure

Fig. 2 Experimental equipment: **a** high-temperature furnace; **b** LF-NMR tester; **c** schematic view of the experimental system



The 8-channel PCI-2 full-digital acoustic emission monitoring system, developed by the American Physical Acoustics Company, was employed in this study (Fig. 3c). In order to avoid affecting the DIC imaging, two probes were taped on the backside of the uniaxial specimen. The acoustic coupling agent was applied between the probe and the rock surface to improve the signal acquisition rate. The sampling frequency is 1 Msps, the gain is 40 dB, and the threshold is 40 dB. Mechanical experiments, 3D digital photographic acquisition, and AE monitoring were carried out simultaneously to ensure data synchronization.

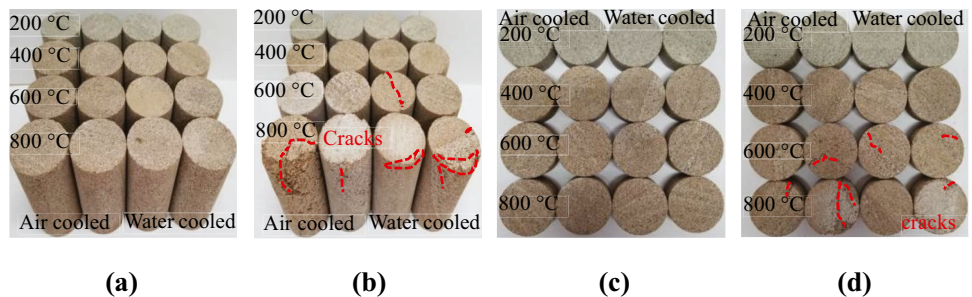
The physical properties of density and P-wave velocity were also measured before and after thermal treatment.

Results and analysis of nondestructive tests

Physical test

Figure 3 is the schematic diagram of the appearance of specimens under different treatment conditions. With the difference in temperature, heating scheme, and cooling method, the apparent color and morphology of the specimens show noticeable differences. The surface color at 200 °C is all light gray, while the color at 400~800 °C is pale reddish-brown. Changes in appearance indicate that the mineral composition of sandstone has altered complexly after heating-cooling treatment.

Fig. 3 The appearance of prepared sandstone with different heating-cooling treatments. **a** Continuously heated cylinder. **b** Periodically heated cylinder. **c** Continuously heated Brazil disk. **d** Periodically heated Brazil disk



Furthermore, when the temperature rises, the surface of the thermal-treated specimen gradually becomes rough and even initiates macrocracks. Naked eyes can observe no macrocracks on the surface of specimens at 200 °C and 400 °C, but numerous microcracks have been induced (Heuze 1983). When the heating temperatures rise to 600 °C and 800 °C, the macrocracks can be observed visibly by the naked eye (Fig. 3b, d). The periodic heating–cooling specimens (A2 and W2) have more severe damage than the continuous ones (A1 and W1). And the water-cooled specimens (W1 and W2) have more obvious macroscopic damage than air-cooled ones (A1 and A2). The density was measured based on mass and volume, listed in Table 1.

Figure 4 shows the variation in porosity with temperature. The A1 sample shows a 2.9% reduction in porosity from 200 to 400 °C. On the other hand, the porosity increases monotonically with the temperature for the periodically treated specimens A2, W1, and W2. The porosity growth of A2 is less than that of W2. At 400 ~ 600 °C, the increasing porosity trend becomes more visible. At 200 °C, the porosity of A2 and W2 is smaller than that of A1 and W1, respectively. With the increase of temperature, the porosity of the periodic heat treatment sample is larger than that of the continuously heated sample. In addition, the results of porosity changes also show that the difference between the porosity of 2A and 1 W is relatively close at the same temperature. The detailed measurement data are summarized in Table 1.

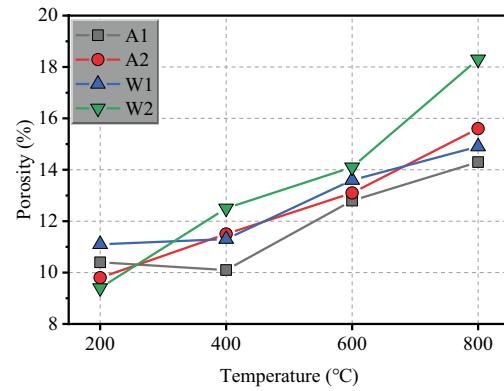


Fig. 4 Porosity varies with temperature under different treatments

Ultrasound characteristics

Ultrasonic wave velocity is widely used in the characterization of thermal cracking and the quantification of overall damage. The average P-wave velocity (V_p) of specimens treated by different methods was measured and plotted in Fig. 5. V_p tended to decrease with the temperature increase. V_p attenuation amplitude of periodic heating specimen is more significant than continuous heating. With the same heating scheme, the V_p of the water-cooled specimen is lower than that of the air-cooled one. By comparing A2-200 and W1-200, the V_p of A2 is higher than that of W1. For example, at 200 °C, V_p of A2-200 is 2.9% higher than

Table 1 The physical and mechanical properties of sandstone specimens after different thermal loading

Specimen	Thermal loading scheme	Heating time	Cooling medium	ρ (g/cm ³)	V_p (m/s)	φ (%)	σ_{t1} (MPa)	σ_{t2} (MPa)	Ucs_1 (MPa)	Ucs_2 (MPa)
A1-200	Continuous heating–cooling (1A group)	1 × 10 = 10 h	Air	2.36	2439	10.4	2.54	2.48	44.3	41.0
A1-400				2.36	2300	10.1	2.75	2.37	57.2	68.2
A1-600				2.30	1399	12.8	1.78	1.51	42.8	38.7
A1-800				2.31	1243	14.3	0.98	1.16	37.0	17.4
A2-200	Periodical heating–cooling (2A group)		Water	2.35	2354	9.8	2.17	2.31	50.0	55.6
A2-400				2.36	2151	11.5	2.21	2.15	35.0	45.7
A2-600				2.33	1191	13.1	1.13	1.41	26.6	34.1
A2-800				2.31	719	15.6	0.43	0.78	19.1	29.1
W1-200	Continuous heating–cooling (1 W group)	5 × 2 = 10 h	Air	2.35	2273	11.1	2.12	2.56	42.6	53.1
W1-400				2.34	2106	11.3	1.96	1.84	38.4	50.5
W1-600				2.31	1369	13.6	1.46	1.53	29.0	49.9
W1-800				2.32	1193	14.9	0.50	0.90	23.5	31.4
W2-200	Periodical heating–cooling (2 W group)		Water	2.36	2128	9.4	1.94	2.32	48.9	63.5
W2-400				2.35	1651	12.5	1.87	1.45	19.3	24.9
W2-600				2.32	345	14.1	0.52	0.75	13.1	23.7
W2-800				2.24	139	18.3	-	-	7.6	0.2

ρ average density of disc and cylinder specimens, V_p longitudinal wave velocity, φ porosity, σ_t tensile strength, ucs uniaxial compressive strength.

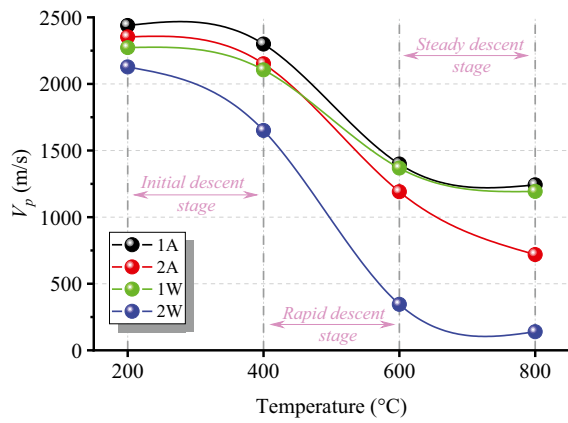


Fig. 5 Variation in V_p of sandstone after different thermal loading schemes

V_p of W1-200. However, the situation is the opposite at higher temperatures (600 °C or 800 °C). When the temperature is 800 °C, V_p of W1-800 is 13.7% higher than V_p of A2-800. This indicates that, at lower temperatures, the cooling method has a more significant impact on the rock than the heating scheme. The higher the temperature, the more

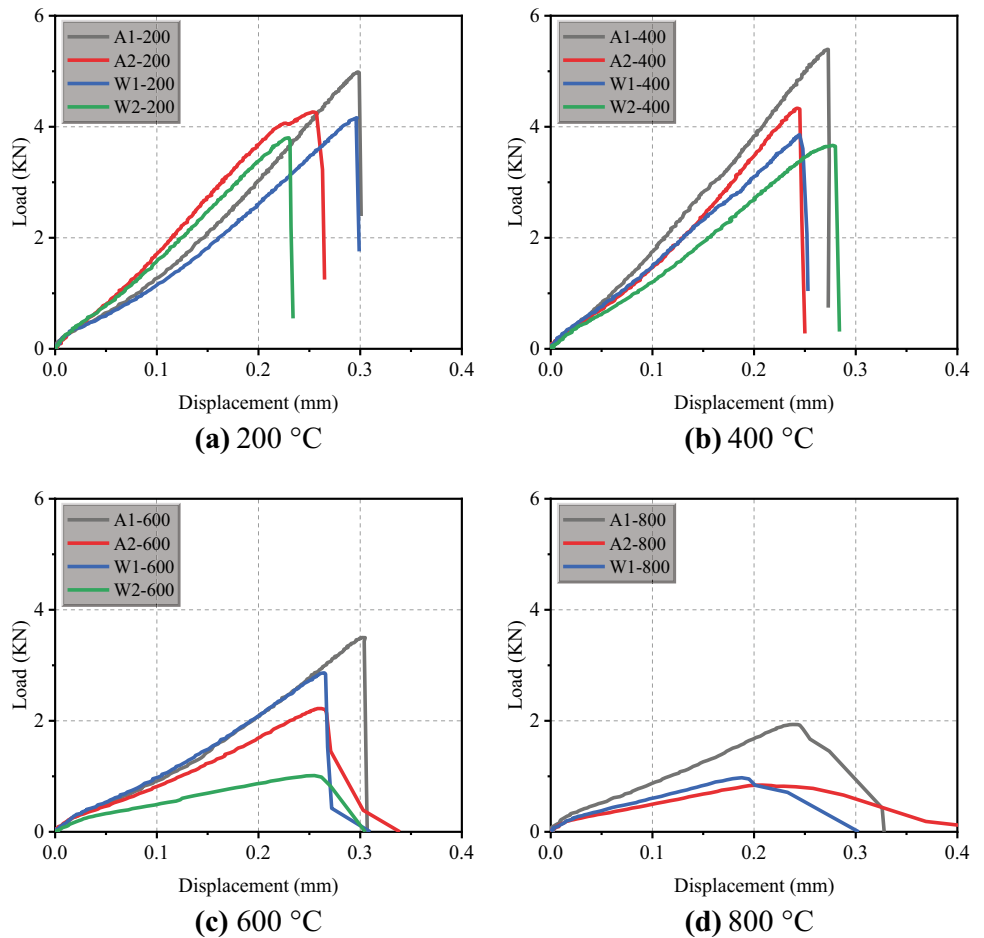
micro-defects generate by periodic heating, which results in V_p of A2-800 lower than that of W1-800.

Results and analysis of Brazilian splitting tests

Load–displacement curve

Figure 6 shows the representative load–displacement curve of the BTS test after continuous and periodic thermal treatment. Although all the curves have compaction, elastic, and yield stages, the post-peak is pretty different. When the temperature is 200 °C or 400 °C, the post-peak stress decreases sharply, which shows obvious brittleness. With the temperature increasing to 600 °C, the load–displacement curves of A2 and W2 show a slow downward trend after the peak value, showing a progressive failure. It can be concluded that the specimens show less brittle failure characterized replaced sudden and brittle failure by considering the load–displacement responses and the post-failure condition. However, the specimen heated continuously at the same temperature still exhibits brittle failure characteristics. At 800 °C, the stress gradually decreases after the stress reaches the peak value for all specimens, and the displacement continues

Fig. 6 Comparison of load–displacement curves of Brazil splitting test under different treatment conditions



until the disk is completely fractured. Note that mechanical data of W2-800 could not be collected because of intensive damage.

Tensile strength

Figure 7 shows the BTS subjected to various treated specimens. In stage 1 (200~400 °C), the σ_t of A-1 and W-1 increases with the temperature, consistent with previous research results (Chen et al. 2012; Ding et al. 2016; Ranjith et al. 2012). The V_p does not have similar evolution may be the difference in filling medium in pores and microcracks, as detail analysis in Sect. 6.3. However, the strength of the periodic heating specimens decreases with the temperature increase from 200 °C to 400 °C. When the temperature increases to 600 °C and 800 °C (stage 2), the σ_t of all cases decreases.

The BTS of periodic heating-cooling specimens is smaller than that of continuous ones. And the reduction in split strength caused by constant heating is smaller than that caused by periodic heating. For A1, the strength declines by 57.4% from 200 to 800 °C, while the strength of specimen A2 declines by 72.8%. For the water-cooling group, σ_t of W1-800 decreased by 70.1% compared with that of W1-200. The damage to W2-800 was too severe to measure the tensile strength. This means the specimens subjected to periodic heating lose more strength than continuous heating, and σ_t of the water-cooled Brazilian disc decreased compared with the air-cooled ones.

Results and analysis of uniaxial compression test

Stress-strain response

Figure 8 shows the complete stress-strain curves of sandstone with various treatments. The stress-strain curves

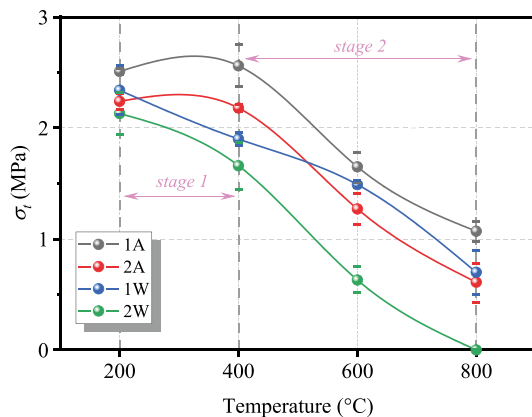


Fig. 7 The variation of splitting strength with temperature under different treatment conditions

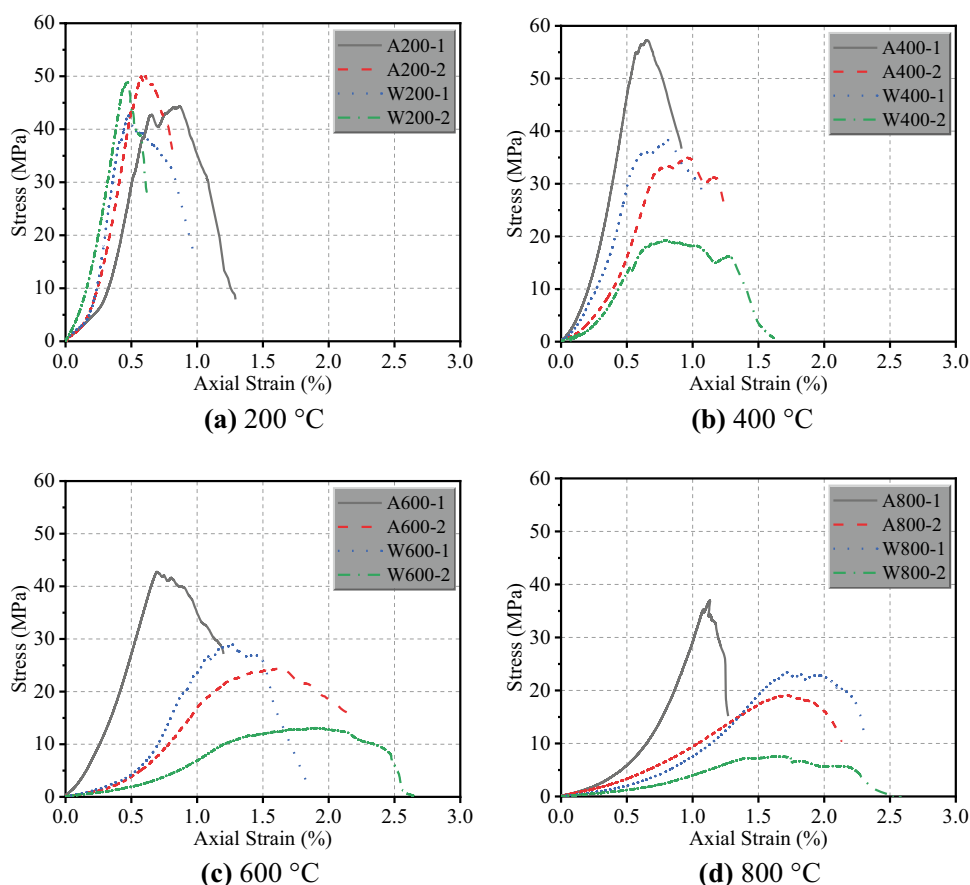
have the compaction stage, elastic deformation stage, stable crack growth, unstable crack growth, and post-peak stage (Martin and Chandler 1994). At the initial loading phase, the stress moderately grows with the increase of strain associated with the closure of the pores and microcracks. Therefore, this stage presents an upward concave curve. As the loading increases, the stress increases linearly with the strain. It is generally believed that no new microcracks generate at this stage. After the elastic deformation stage, new cracks in the specimen continuously initiate, extend and coalesce until the bearing limit. The strain softening occurs after the stress exceeds the peak strength, and the stress decreases with the increase of the strain, indicating that the internal structure is failed. The crack develops rapidly in this phase until the specimen is completely fractured.

Figure 8a shows little difference in the deformation characteristics of the five stages among the curves of different specimens for the heating scheme at 200 °C. After passing the brief compaction stage, the stress increases linearly with strain. The strain-softening segment of the curve after the peak is short. At 400 °C, the nonlinear phase of stress growth is prolonged. Note that W2-400 has completely different stress-strain characteristics, reflected in the softening stage after the peak is extended (Fig. 8b). As the temperature further increases to 600~800 °C, the failure of sandstone becomes more complicated. The stress increment corresponds to a more significant strain increment. The compaction stage is longer than that of the specimen heated at 400 °C, showing a typical upward concave curve. The curve shifts to the right, corresponding to a significant increase in peak strain, as seen in Fig. 8c, d.

Compressive strength and deformation parameter

Figure 9 presents the UCS of sandstone after thermal treatments vary with temperature. The strength of the periodic heating and W1 specimens decreases with the temperature, whereas the UCS of the A1 first increases and then decreases. The difference mainly appears in the range of 200 °C to 400 °C: The UCS of A1-400 is increased by 29.1% than that of A1-200. This is consistent with the research results of Ding et al. (2016) and Ranjith et al. (2012) on sandstone and Chen et al. (2012) on granite. The periodic thermal treatment has the opposite effect on UCS, resulting in a 30.0% decrease in UCS of A2-400 compared to A2-200. The V_p evolved differently with UCS, which is explained in Sect. 6.3. The periodic heating schemes degenerate more than continuous heating on the strength. At the same temperature, the UCS of periodic heating-cooling groups (2A and 2W) is always inferior to that of continuous ones (1A and 1W). And the gap

Fig. 8 Stress versus strain relationship of the sandstone for different thermal treatments



between the two increases as temperature increases. The strength decline of A1-200 to A1-800 is similar to that of W1-200 to W1-800. The UCS of A2-800, however, reduced by 61.8% from A2-200, and the UCS of W2-800 dropped by 84.5% from W2-200. At the same time, It can be found that the UCS loss of A2 and W2 samples mainly occurs at 200~400 °C, indicating that even at low and medium temperatures, periodic thermal action will have a non-negligible impact on the mechanical properties of rock.

With increasing temperature, Young's modulus (E) also exhibits the same tendency as UCS (Fig. 9). For A1 specimen, E slightly increases when the temperature is up to 400 °C and then starts to degrade from 400 to 800 °C. The situation is different for A2, W1, and W2 specimens subjected to periodic treatment, where a continuous reduction in E is observed with increasing temperature. After heating at the same temperature, E of the periodically treated specimen is less than that of the continuously treated sample, and the E of the water-cooling specimen is less than that of the air-cooling one.

The reduction of E can be considered due to the decrease in strength and weakening resistance to deformation. DIC images obtained close to the peak stress can also further confirm the weakening of the deformation

resistance ability. Figure 10 shows the strain field distribution on the specimen surface under different thermal treatments. In the zone of interest (ZOI), the purple region represents the low strain, and the red region means the high strain. The lateral strain field captured from the sandstone surface can be observed that specimens that suffered more damage bear more deformation at critical failure. In addition, splitting failure can be observed in the sandstone specimens heated at 200 °C. However, shear failure occurred when the temperature continued to rise, accompanied by multiple shear planes. And due to the stimulation of thermal fatigue and water cooling, the shear failure feature is more evident in periodic heating samples, which results in complex failure. Specimens A2-800 and W2-800 were fractured along the main shear plane, showing a characteristic of general shear failure.

AE behavior

The AE characteristic parameters can infer the damage and failure of rock because it is closely related to the cracking behavior of dislocation motion, grain boundary movement, or closure, initiation, propagation, and coalescence (Eberhardt et al. 1998). Acoustic emission characteristics of sandstone were analyzed by AE counting in the loading

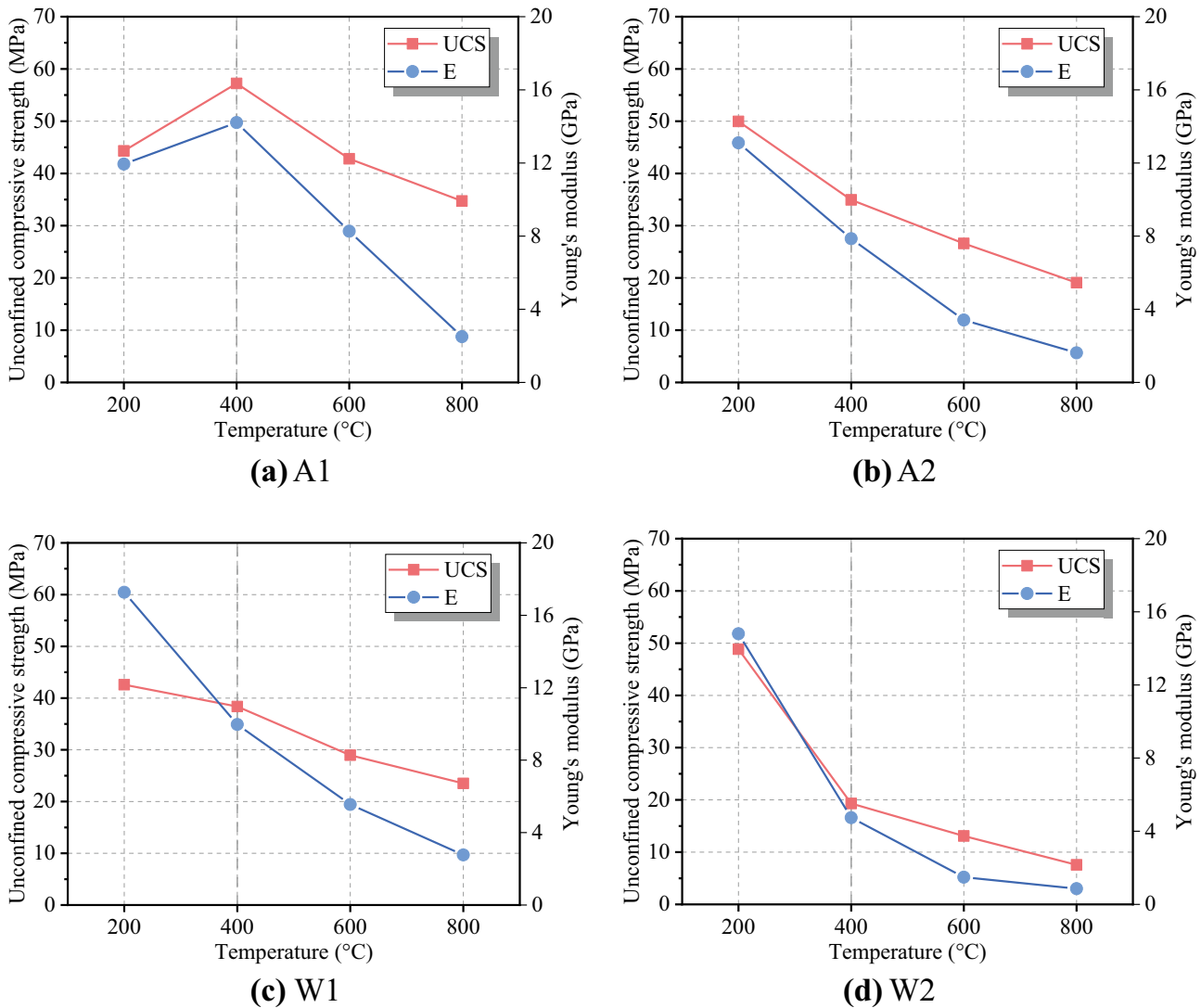


Fig. 9 UCS and Young’s modulus for different thermal treatments

process and cumulative acoustic emission counting (Zhao et al. 2022b), as shown in Fig. 11. Four specific points are marked on the stress–strain curve: A, B, C, and D based on the AE events evolution. Point A is where the AE event increases above the event background level for the first time, after which the AE counts increase steadily. B corresponds to the beginning of an unstable increase in the AE counts. C is the peak stress point, and D is the turning point of the accumulation counts curve in the post-peak stage. The generation of AE activity before point A is related to the closure of the pre-existing microcracks inside the rock (Sha et al. 2020). At 200 °C, almost no AE signal is monitored for the various heating scheme and cooling method specimens during initial loading. This implies that only very few thermally induced microcracks are initiated inside the specimens at this temperature. For specimens heating at 400 °C, AE counts appear in the

initial loading stage, which means an increase in closure and extension of micro-defects formed by thermal treatment. In addition, this phenomenon in the water-cooled specimens is more prominent than in the air-cooled ones, and the periodically heated specimens are more evident than the continuous ones. AE counts are more distributed when the temperature rises to 600 °C and 800 °C. The AE counts appear at the beginning of loading and increase gradually, but the peak of counts is no longer prominent when the rock fractures.

When the rocks are fractured, the AE counts of rocks at normal temperature usually increase suddenly and drop rapidly. After heating–cooling treatment, the signal active time in the post-peak stage is prolonged (Fig. 11). All samples belong to brittle failure at 200 °C, but in the post-peak stage of the periodic specimen (A2-200 and W2-200), the counts distribute more. At the same time, the failure of sandstone after

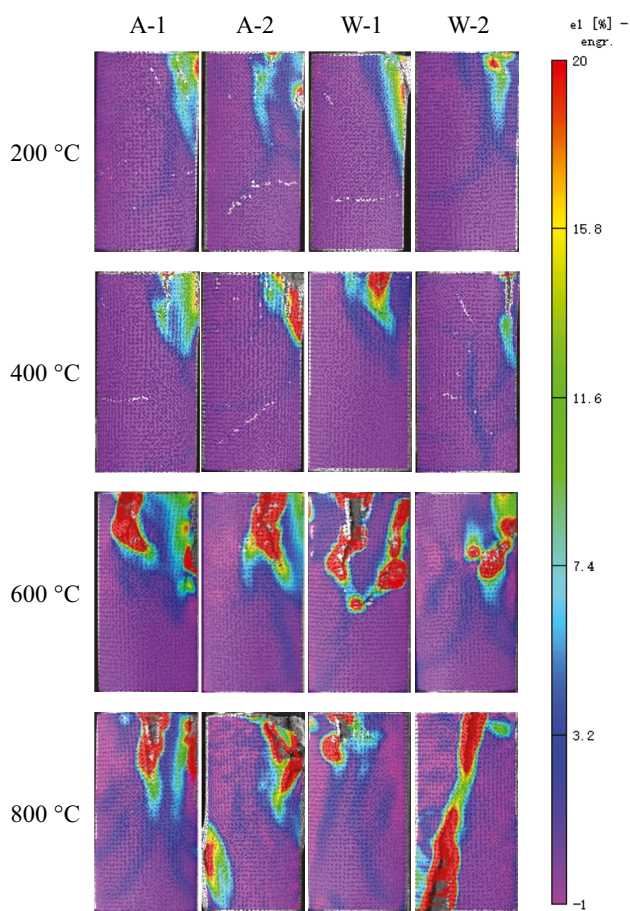


Fig. 10 Lateral strain distribution of uniaxial test at failure based on DIC

heating–cooling treatment at higher temperatures occurred more ductile. Numerous AE events occur in the post-peak stage, showing a brittle-toughness transition e.g., W2-600 (Fig. 11l), A2-800 (Fig. 11n), and W1-800 (Fig. 11o). This is because the damage increases to a high level, e.g., the distribution of thermal-induced microcracks throughout the specimen and the evolution of macrocracks (Yin et al. 2019). Note that in the large deformation of the specimen W2-800 during the loading process, the probe is in poor contact with the specimen surface, and the AE counts are hardly collected (Fig. 11p).

Discussion on the damaging mechanism of periodic thermal treated sandstone

Pore structure evolution induced by thermal damage

Distribution of T2 spectrum

To quantitatively study the pore distribution and cracking evolution of sandstone, we analyzed the T2 spectrum and pore size distribution. The spectrum curve takes the transverse relaxation time as the X-axis and the relaxation signal

as the Y-axis. According to the porous media relaxation theory and the low-field nuclear magnetism theory, the decay time of the transverse magnetization vector generated by polarization in an external static magnetic field is T2 relaxation time. T2 is related to the restriction of 1H, and the pore structure determines the degree of 1H to be restrained (Xie et al. 2018). The smaller the pore size is, the more restrictive and the shorter the relaxation time is, and vice versa. In porous media, the T2 of the fluid can be expressed as follows (Wang et al. 2022b):

$$\frac{1}{T_2} = \frac{1}{T_{2s}} + \frac{1}{T_{2D}} + \frac{1}{T_{2B}} \quad (1)$$

T2S is the time of surface relaxation of rock particles; T2B is the relaxation time from the liquid itself; and T2D is the relaxation time caused by molecular diffusion. Considering that surface relaxation plays a decisive role, Eq. (2) can be simplified as follows (Matteson et al. 2000):

$$\frac{1}{T_2} = \frac{1}{T_{2S}} = \frac{\rho_2 S}{V} = \rho_2 \frac{F_s}{r} \quad (2)$$

where T_2 is the transverse relaxation time; ρ_2 is the transverse surface relaxation strength; F_s is the geometric factor of pore shape: for tubular pores, $F_s = 2$; and r is the pore radius.

Referring to the research of Hodot (1966) and Hao et al. (2022), we divided the rock pores as follows: nanopores (< 10 nm), micropores (10–100 nm), mesopores (100–1000 nm), and macropores (> 1000 nm). With the increasing temperature, the difference becomes apparent in T2 spectrum (see Fig. 12). The curves of the specimens heated at higher temperatures generally shift to the right compared to those heated at lower. The right shift is reflected in the increase in peak relaxation time (T2peak). The T2peak of A1, A2, W1, and W2 specimens extends from 2.01 ms, 2.01 ms, 1.52 ms, and 2.31 ms at 200 °C to 12.33 ms, 12.33 ms, 12.33 ms, and 57.22 at 800 °C, respectively. This indicates that the size of the dominant pore expands. The T2max of A1, A2, W1, and W2 specimens extends from 2.67 ms, 2.01 ms, 1.52 ms, and 2.31 ms at 200 °C to 15.31 ms, 12.33 ms, 12.33 ms, and 57.22 at 800 °C, respectively (Table 2). In addition, the T2 spectrum of the four groups presents a unimodal pattern, which differs from the dual peak distribution in A1, A2, and W2 specimens at 800 °C. Changes in the curve shape indicate that the pore structure changes from uniformity to complexity, that is, there are not only large cracks and pores formed by expansion and penetration but also nanopore and micropore newly initiation. This is a dynamic evolutionary process. The initiation of new cracks accompanies the expansion of existing pores, and the continuous appearance of micro defects promotes the interaction between microcracks and pores,

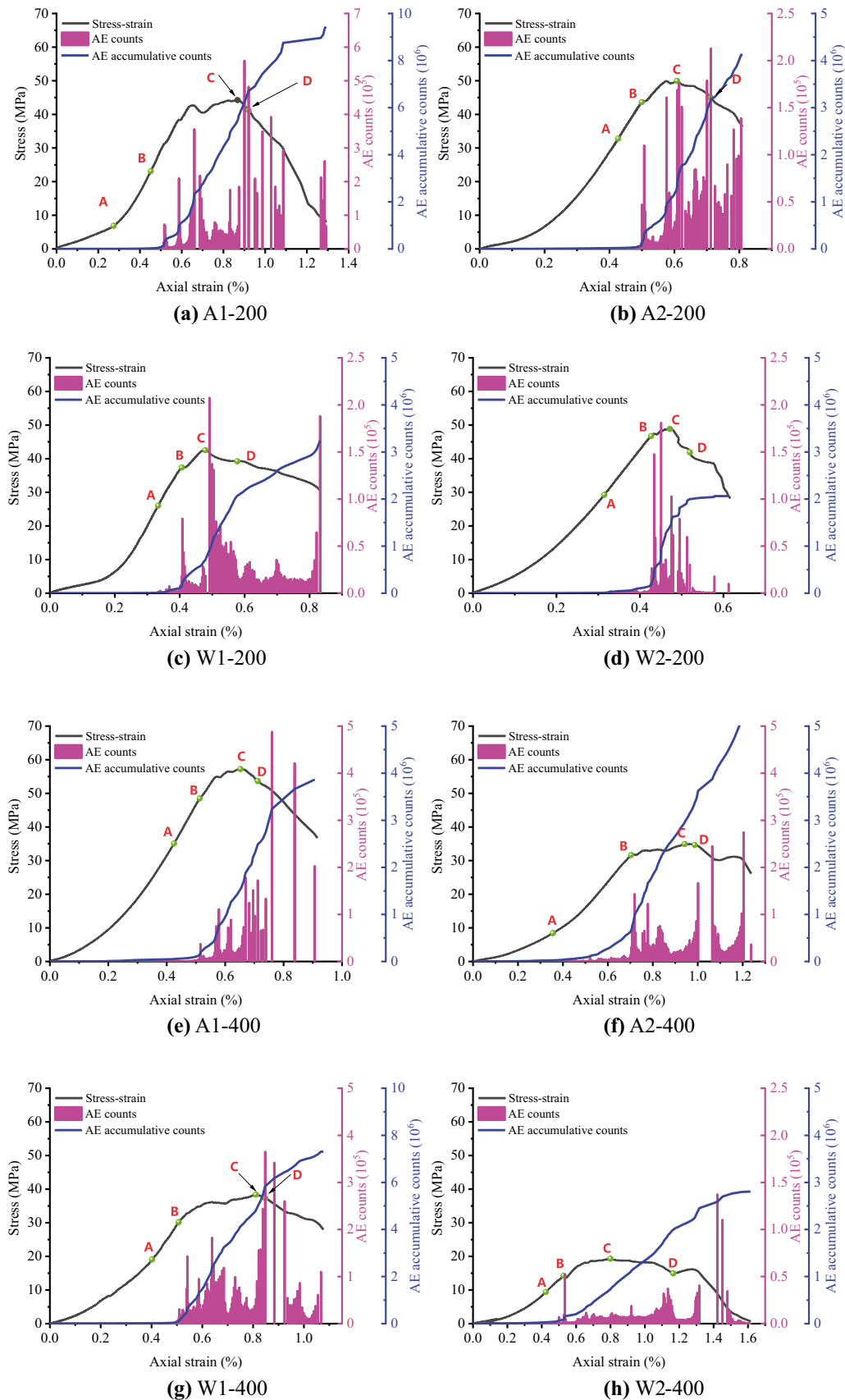


Fig. 11 Evolution of AE count and cumulative AE counts for sandstone specimens exposed to different thermal treatments

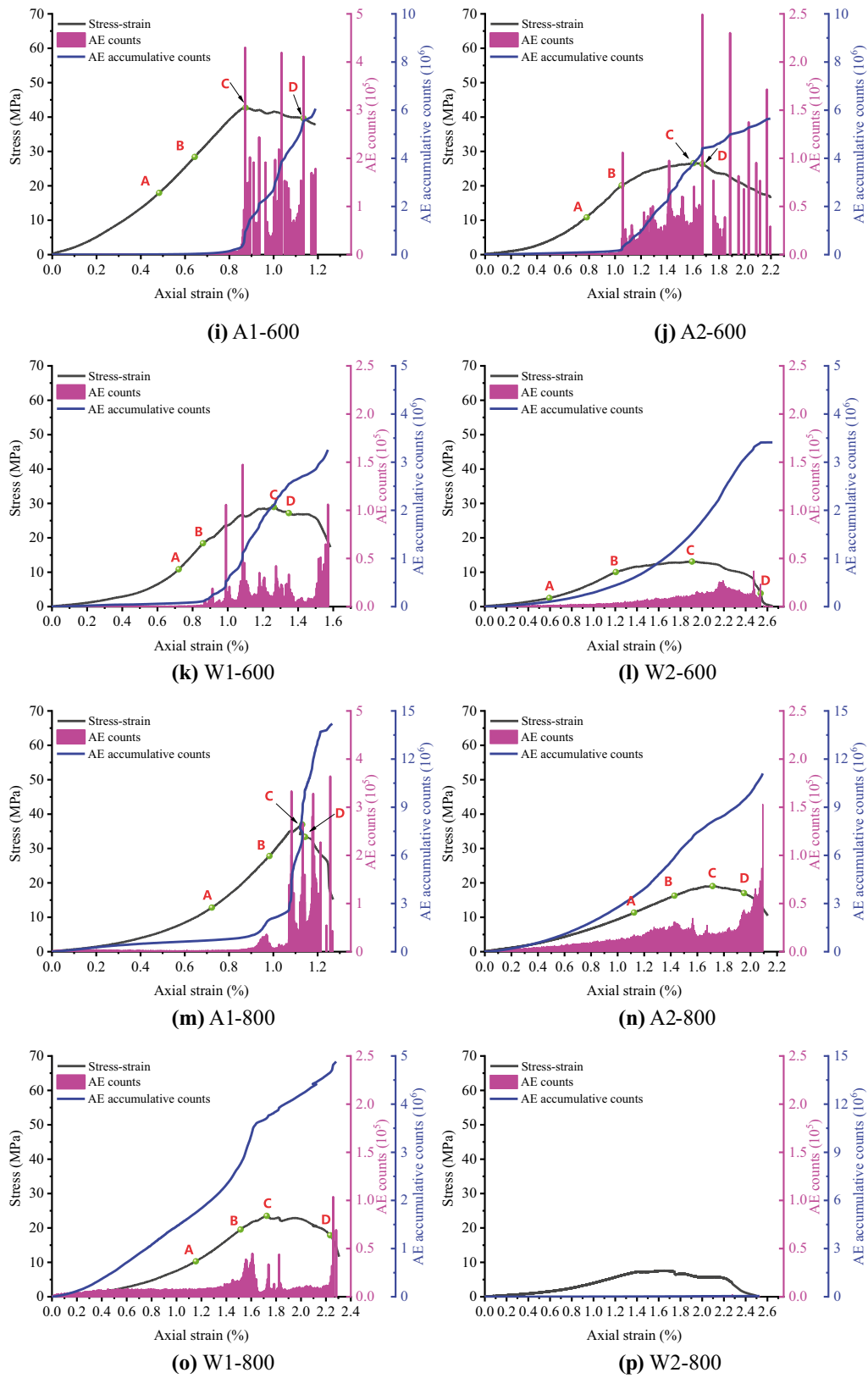


Fig. 11 (continued)

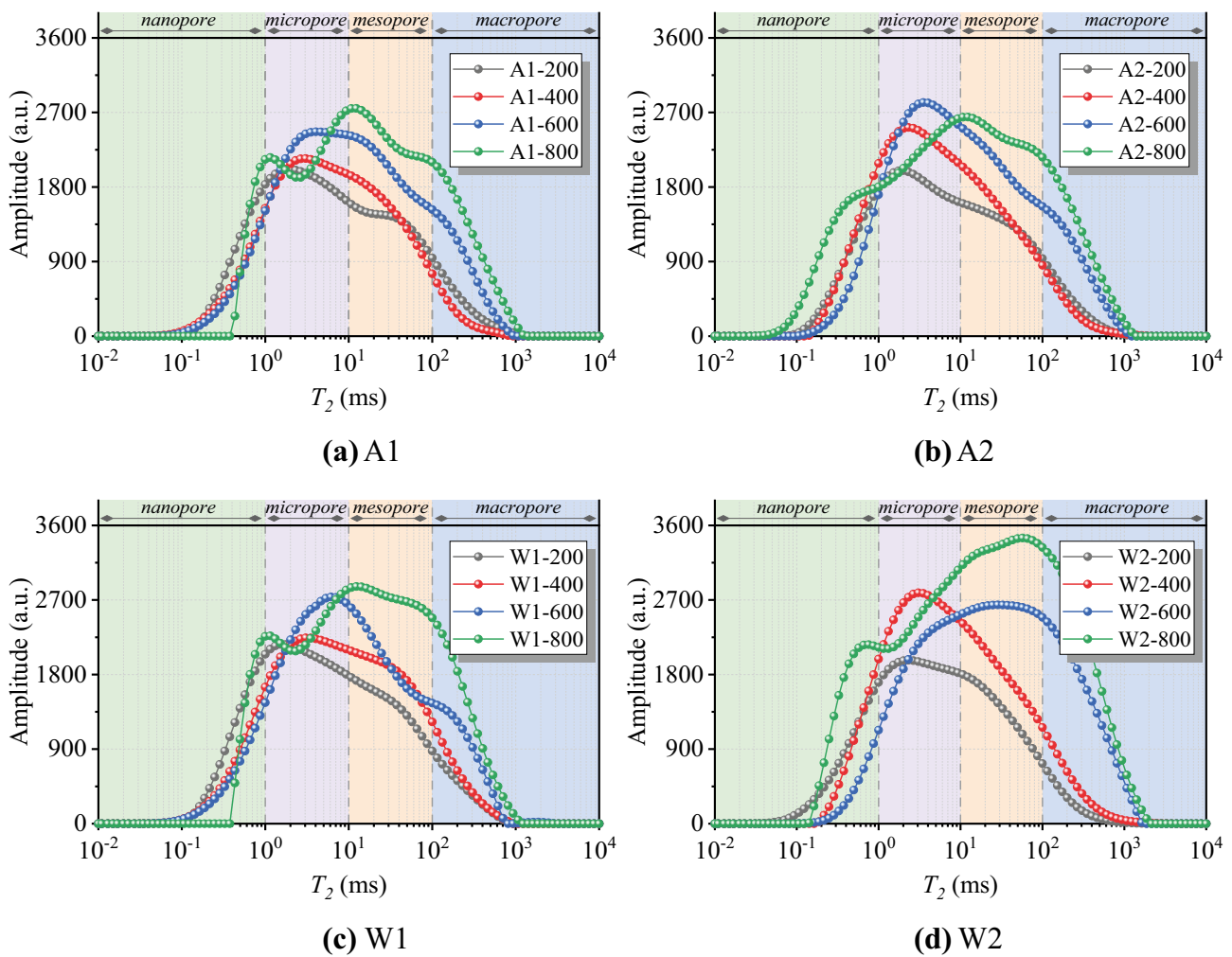


Fig. 12 The distribution curve of the T2 spectrum under different thermal treatments

leading to the constant growth of peak area (see Table 2). For example, in the W2 group, the peak area (A) of the W2-800 is 155899, which is 120% higher than that of the W2-200 (70,836).

Then, consider the effect of periodic heating–cooling treatment on the T2 spectrum. The multiscale pore peak area in periodic thermally treated samples at 200 °C decreases, except for A2 nanopores (Fig. 13a). At 400 °C, compared with A1 and W1, the increased pores of A2 and W2 are mainly nanopores and micropores (Fig. 13b). At 600 °C, one significant variation is the micro-to-macro transform in the pores of specimen W2-600. It is generally considered that the water signal corresponding to the relaxation time of more than 1000 ms is the free water that exists in the macroscopic fractures. Due to repeated phase transitions and thermal shocks, the pores and microcracks expand, converge, and penetrate, dramatically increasing the peak area of the mesopore and macropore (Fig. 13c) but also forming macroscopic fractures. The difference between the samples

of water cooling combined with the air-cooling group after 600 °C treatment is caused by thermal shock. Thermal shock is more likely to form surface cracks, which provides an advantageous channel for the immersion of cooling media. Water goes deep into the specimen along the gap and continues to undergo rapid heat exchange in the track. This thermal gradient deep into the interior constantly stimulates the rapid deterioration of the rock structure surrounding the fracture. At 800 °C, the peak area of the micropore, mesopore, and macropore in A2 is slightly larger than that in A1, while the peak area of the nanopore in A2 is significantly larger than that in A1 (Fig. 13d). This indicates that in repeated thermal heating, the expansion, propagation, and coalescence rate of the existing pores in the periodic and continuous heating samples are similar, but the extreme increase of nanopore induced by fatigue effect is observed. Compared with W1-800, the peak areas of multiscale pores, especially nanopore and macropore, increased pronouncedly after periodic heating and water cooling.

Table 2 The representative relaxation times and peak areas of sandstone specimens after periodic thermal treatments

Specimen	T_{2min} (ms)	T_{2max} (ms)	T_{2peak} (ms)	A_n	A_i	A_e	A_a	A
A1-200	0.107	1232.847	2.01	12003	30428	23926	6455	72811
A1-400	0.015	811.131	2.70	9013	31935	26113	3860	70922
A1-600	0.017	932.603	4.04	8070	35840	34747	13187	91845
A1-800	0.433	1232.847	12.33	7743	34710	41339	20639	104431
A2-200	0.081	1232.847	2.01	12137	29685	23700	6367	71888
A2-400	0.142	2154.435	2.31	12115	37607	26575	5193	81491
A2-600	0.093	1072.267	3.51	7627	40470	35450	15097	98644
A2-800	0.015	1232.847	12.33	21167	35005	41634	21163	118969
W1-200	0.093	811.131	1.52	14065	32694	24921	6292	77972
W1-400	0.017	932.603	3.05	9671	33634	31434	7997	82736
W1-600	0.015	2848.036	6.14	8343	37216	34124	13979	93662
W1-800	0.433	1072.267	12.33	9007	37138	46612	22063	114820
W2-200	0.015	3764.936	2.31	12399	30327	23955	4155	70836
W2-400	0.187	4328.761	3.05	9593	41130	32323	7998	91044
W2-600	0.035	1629.751	28.48	4307	31970	44178	29167	109622
W2-80	0.142	1873.817	57.22	19614	39635	56482	40158	155889

T_{2min} , T_{2max} , and T_{2peak} represent the minimum, maximum, and peak transverse relaxation time, respectively, A_n , A_i , A_e , A_a , and A represent the T_2 peak areas of the nanopore, micropore, mesopore, macropore, and all pores, respectively

The multiscale porosity in sandstones with different thermal treatments is counted in Fig. 14, according to the classification in pores size. The histogram shows that nanopore, macropore, mesopore, and micropore porosity (ϕ_n , ϕ_i , ϕ_e , and ϕ_a) changes dynamically with temperature. At 200~400 °C, the most noticeable change comes from ϕ_i of the periodical sample, that ϕ_i of A2 goes from 4.02% to 5.31%, and W2 changes from 4.04% to 5.71%. The porosity of other pores does not change much. The four porosities A2 and W2 are less than A1 and W1, respectively. After heating at 600 °C, ϕ_n of A1, A2, and W1 decreases, while the porosity of the other three pores enlarges. However, ϕ_i of W2 also decreases. This transition indicates that the formation rate of larger pores is faster than that of new small cracks and pores at this temperature, especially W2.

The pore evolution of the samples treated at 800 °C is different from 600 °C. For continuous heating samples A1 and W1, ϕ_n slightly increased, ϕ_e and ϕ_a significantly increased, but ϕ_i decreased. The initiation rate of new cracks is faster than the transformation rate of small to large pores. For periodic heating samples A2 and W2, ϕ_n increases more significantly. This indicates that periodic heat treatment has a more significant stimulation on the formation of microcracks under the same heating time. At the same time, numerous nanopores induced by cracking create conditions for the expansion, connection, and coalescence of pores, ultimately leading to an increase in ϕ_e , ϕ_a , and ϕ . Therefore, the total porosity and the differences in multiscale pore structures should be considered when considering the effect of porosity on mechanical properties. For example, there is little

difference in ϕ between W2-600 and A1-800, but ϕ_e and ϕ_a of W2-600 are significantly more than those of A1-800, which makes the mechanical properties of W2-600 degrade more seriously.

To characterize the uniformity of pore distribution, Wichtmann and Triantafyllidis (2013) proposed the uniformity coefficient concept in pore size, referring to the uniformity coefficient in soil particle size (Eq. (3)):

$$C_u = \frac{d_{60}}{d_{10}} \quad (3)$$

where C_u is the uniformity coefficient of pore size; d_{10} is the pore diameter at a cumulative pore proportion of 10%; d_{60} is the pore diameter at a cumulative pore proportion of 60%.

According to Jia et al. (2020), ρ_2 in Eq. (2) is considered 5 $\mu\text{m/s}$, and we use Eq. (2) to convert the transverse relaxation time into the pore radius. By dividing the amplitude corresponding to each pore radius in the T2 spectrum by the total amplitude (A), the proportion of the pore volume corresponding to the pore radius to the total pore volume can be obtained. The cumulative pore size curves were obtained by accumulating the pores of different sizes. The longitudinal axis presents the pore volume proportion, and the X-axis corresponds to the pore radius, as shown in Fig. 15.

The variation of C_u with temperature calculated according to Eq. (3) is shown in Fig. 16. In the first stage (200~400 °C), C_u of A1, A2, and W2 decreases. According to the definition of soil gradation index, the larger the C_u , the more nonuniform the pore structure distribution.

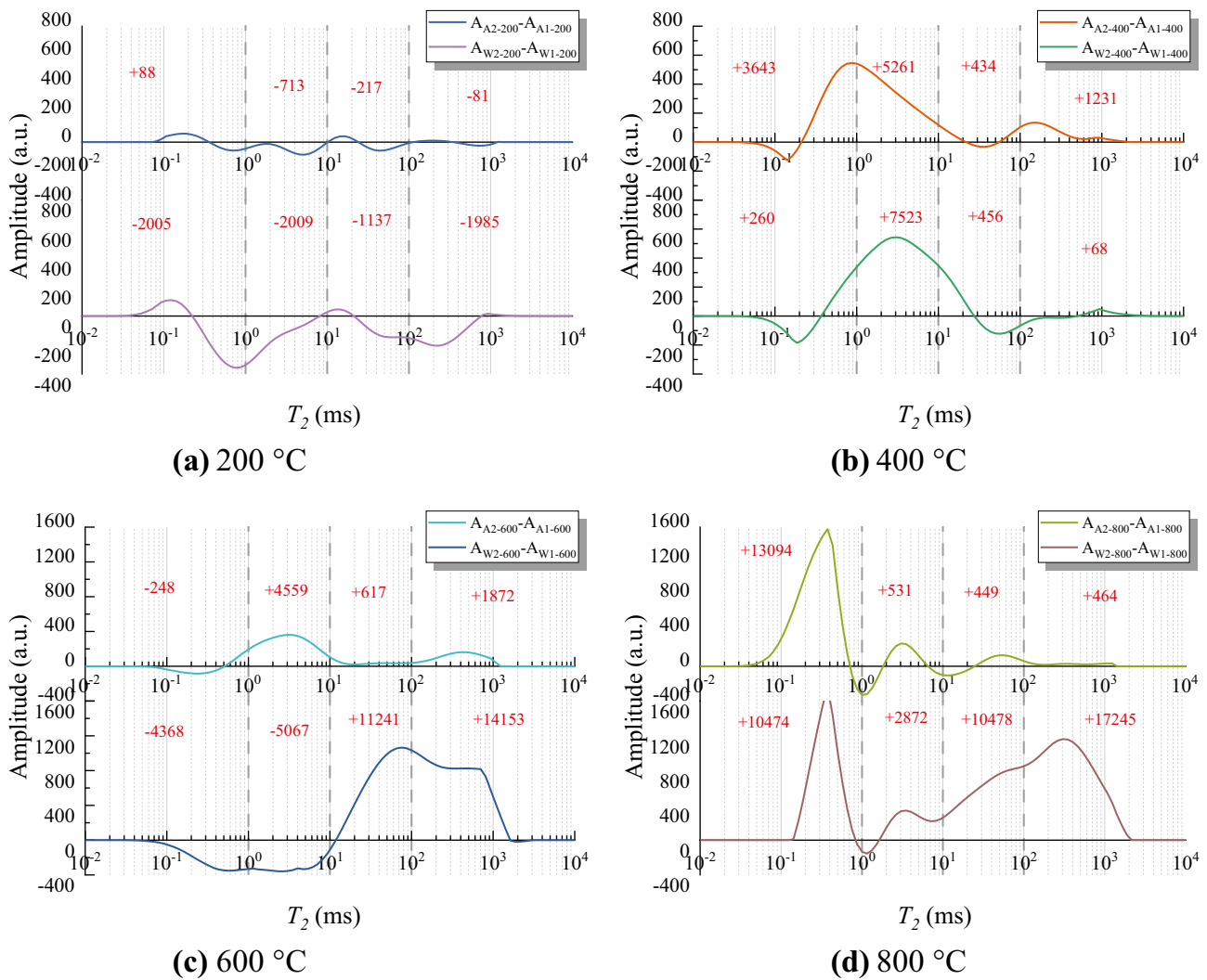


Fig. 13 The increment of the peak area of periodically heated samples compared with that of continuously heated samples

The decrease may be due to the tendency of pore closure caused by thermal-induced enhancement. Thus, the uniformity of pore distribution is improved to some extent.

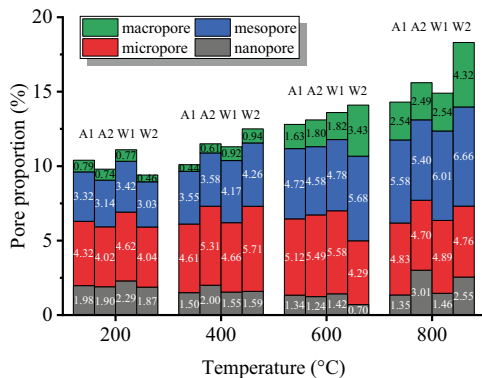


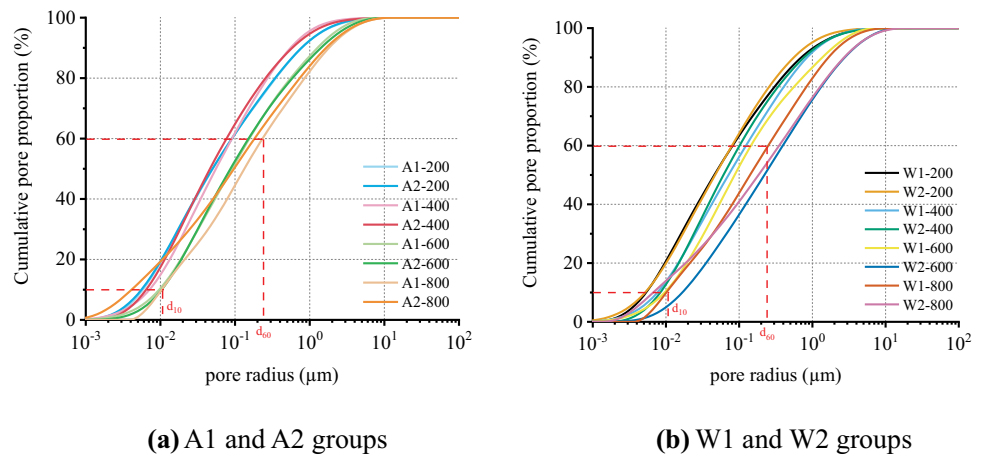
Fig. 14 The porosity of nanopore, micropore, mesopore, and macropore proportions in the thermally treated sandstone specimens

Note that this does not imply a specific decrease in porosity, as there is also the appearance of new cracks and the expansion of internal defects. As the temperature increase to 600~800 °C, Cu of A2 and W2 increase rapidly, and Cu of A1 and W1 increase gradually, indicating a more uneven pore structure is stimulated by periodic thermal treatment.

Magnetic resonance imaging

Figures 17 and 18 show the two-dimensional magnetic resonance imaging (MRI) projections of A2-600 and W2-600, respectively. Seven sections are selected along the height direction for imaging, and five sections are chosen along the radial direction for imaging. Within the range of the specimen image, the red spot presents a high proton density, indicating a strong 1H signal. The blue area gives a low proton density, indicating a poor 1H signal. This means the more red spots aggregated,

Fig. 15 Cumulative pore size distribution curves for samples



the brighter they are, and the more pores and cracks. The results show that W2-600 damage is more severe than A2-600, manifested as the expansion of the red spots area and the enhancement of brightness corresponding to more mesopores and macropores. The blue spots that are more distributed in specimen A2-600 rarely appear in W2-600. This is due to a sharp decrease in nanopores and micropores represented by blue dots, as seen from the pore distribution in the T2 spectrum (Fig. 18a, b). The results of MRI test are consistent with those of the pore structure test and visually describe the difference in damage and deterioration of air-cooled and water-cooled samples during periodic heat treatment. This can be explained by water weakening and thermal shock, combined to determine the internal structure and integrity of the rock treated by periodic heating and water cooling. It will be further elaborated on in Sect. 6.4.

Damage behavior based on AE

AE count is proportional to the energy released by dislocation motion, particle peeling, fracture, and microcracks propagation in the material, based on which it can reveal material

properties (Heiple and Carpenter 1983; Wadley et al. 2013). In the present paper, AE count and AE cumulative count have been utilized as characteristic parameters to describe the damage evolution of thermally treated rocks during loading.

The damage variable (D) can be defined as follows (Tang et al. 1997):

$$D = \frac{N_d}{N_0} \tag{4}$$

where N_d and N_0 are the accumulative AE counts at any damage and accumulative AE counts at rock failure, respectively.

Affected by factors such as insufficient stiffness of the testing machine and different fracture conditions of the rock specimens, it is common for the testing machine to stop prior to being completely fractured ($D = 1$) during the test. Therefore, the predecessors proposed the critical damage value (D_U) to modify the D (Sha et al. 2020):

$$D = D_U \frac{N_d}{N_0} \tag{5}$$

In order to simplify the calculation, the critical damage value is normalized according to the method of linear function conversion (Liu et al. 2009):

$$D_U = 1 - \frac{\sigma_c}{\sigma_p} \tag{6}$$

where σ_c is the residual compressive strength and σ_p is the peak strength.

Combining Eqs. (5) and (6), the rock damage variable D calculated by the AE count can be obtained:

$$D = \left(1 - \frac{\sigma_c}{\sigma_p}\right) \frac{N_d}{N_0} \tag{7}$$

Note that, according to the stress–strain curve, the residual strength in this paper is taken as 0. Thus, we obtain the change of D with axial strain, as shown in Fig. 19.

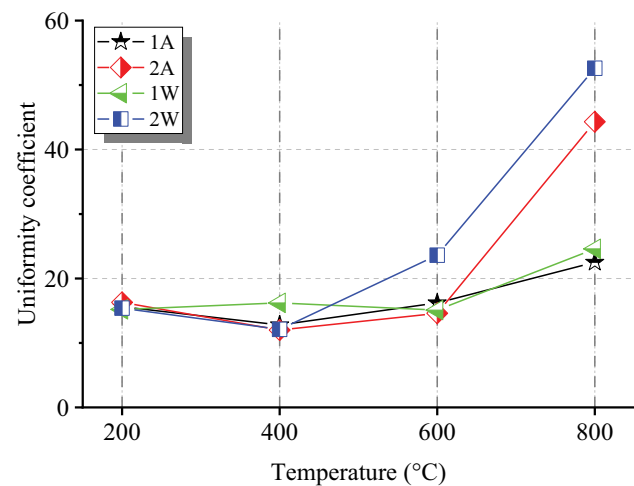
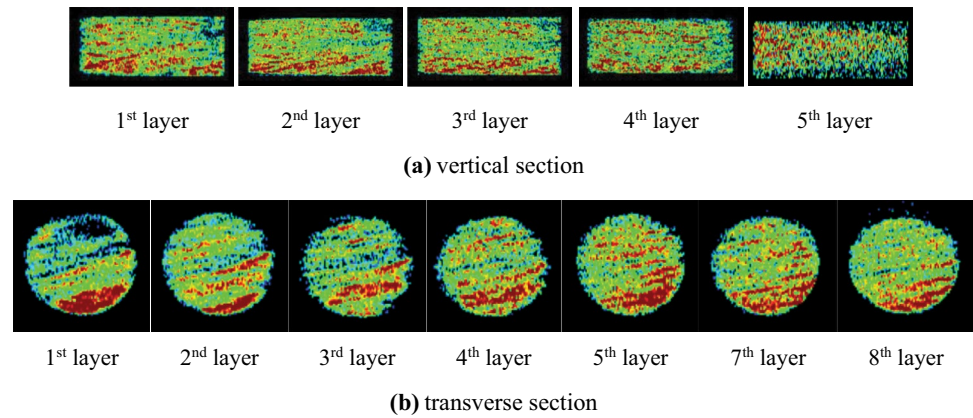


Fig. 16 Variation in Cu with temperature under different treatments

Fig. 17 MRI of A2-600



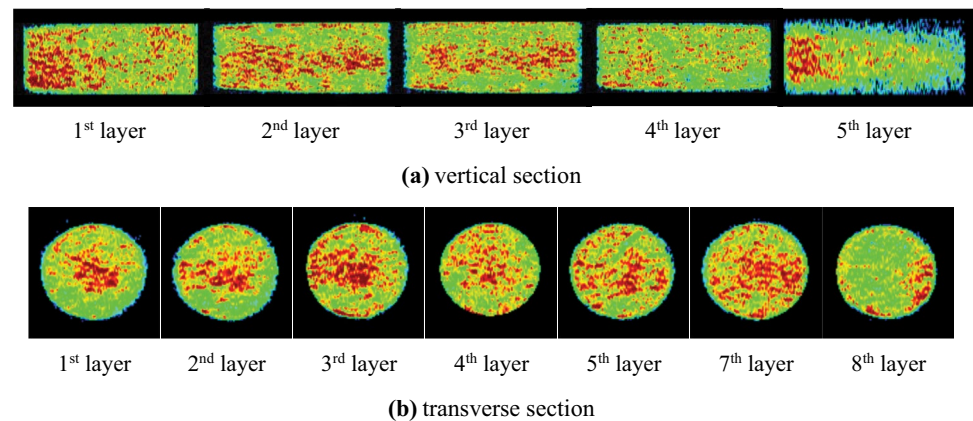
The damage evolution of sandstone during uniaxial compression after different thermal treatments is divided into four stages by three characteristic points A, B, and C. (I) The initial damage stage (before A) basically corresponds to the compaction stage and the early stage in the elastic deformation stage of the stress–strain curve. AE counts in this stage are mainly stimulated by the closure of pre-existing internal micro-cracks, and accumulative AE count accounted for a small proportion of the whole process. For A1, A2, and W1 (Fig. 19a, b, and c) below 800 °C and W2 below 600 °C (Fig. 19d), the damage variable in the first stage tends 0. For W2-600 and the specimen heated to 800 °C, the D value caused by crack closure at this stage increases. (II) With the increase of axial stress, the stress–strain curve progresses to the elastic deformation and stable crack growth stage (AB stage). New microcracks initiate and expand in sandstone, and the pre-existing microcracks develop onset. AE events enter the active phase, that is, the damage development stage, in which the AE counts monitored begin to increase, and the damage variable increases continuously and steadily.

(III) The accelerated damage growth stage (BC stage) corresponds to the yield phase of the stress–strain response. Interactions such as the expansion, convergence, and penetration of micro-cracks within the rock specimen have intensified, and large-scale and numerous new cracks continue

to emerge. Therefore, the AE event enters an outburst state until the AE counts reach the peak, corresponding to the macroscopical fracture. D rises sharply, and the rock specimen damage accelerates. By comparing Fig. 19a, b, it can be seen that the damage variable of A2 at the end of the third stage is greater than that of A1. This implies that water cooling enhances the damage during the thermal process, leading to more monitored AE events caused by crack closure, initiation, expansion, coalescence, and penetration before the peak of mechanical loading. By comparing Fig. 19c, d, it can be seen that the damage variable value of W2 at the end of the third stage is smaller than that of W1, which is because of the ductility failure of W2 increases the proportion of AE events in the post-peak phase. (IV) After reaching the peak strength, the damage variable enters the damage fracture stage (after C). Due to the brittleness of the specimen, the intense AE activity remains in the early post-peak period and then gradually decreases with the further increase of the axial strain. After the rapid growth, D also tends to increase steadily until it reaches 1. It can also be found that the proportion of damage variable of W1 is less than that of A1 in the fourth stage due to the enhancement of the post-peak ductility characteristics of water-cooled specimens.

It is worth mentioning that, at 800 °C, the damage variables of A2 and W1 increase smoothly without an apparent

Fig. 18 MRI of W2-600



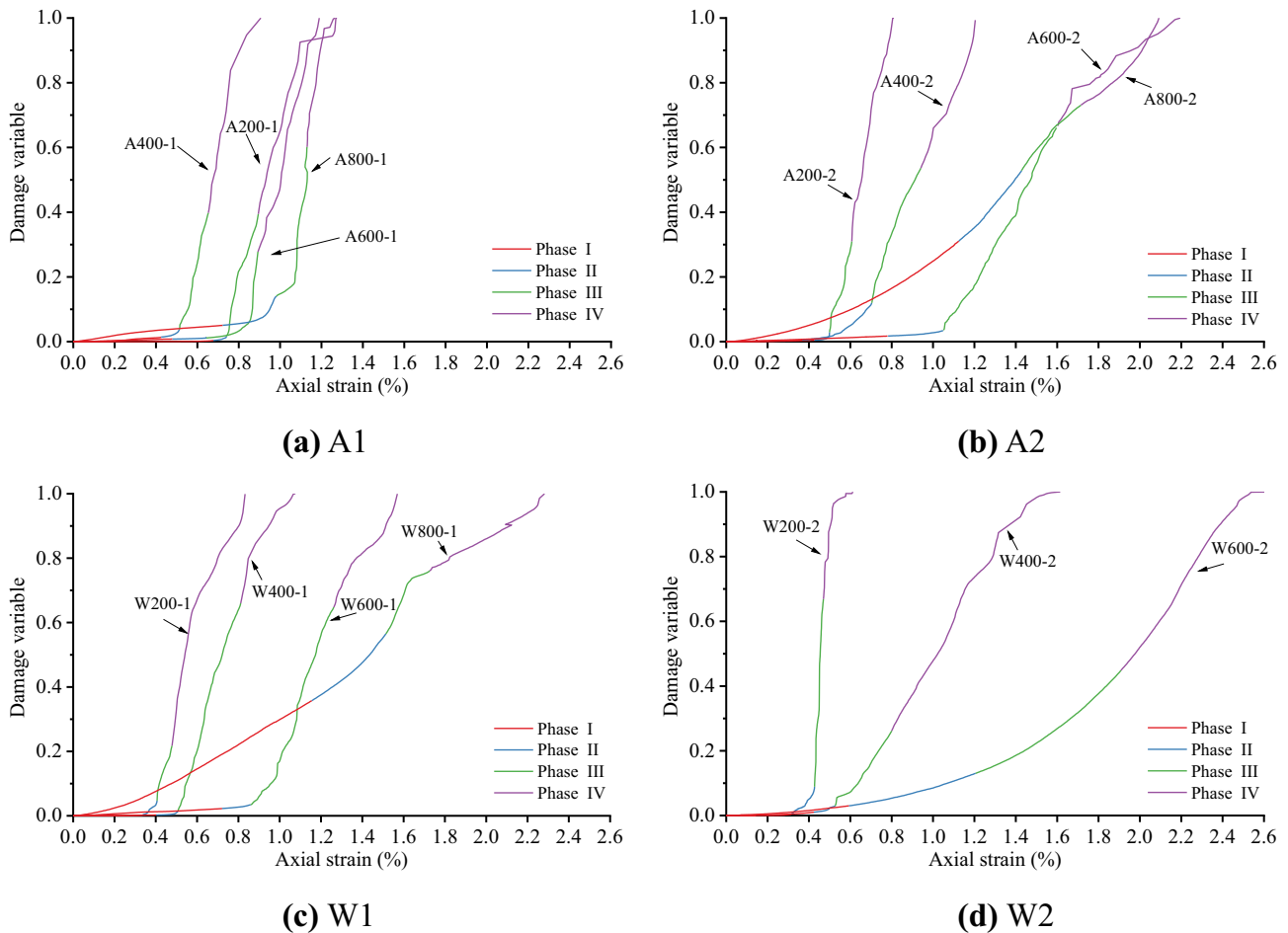


Fig. 19 Evolution of damage variable with axial strain for specimen after different thermal treatments

turning point. This is related to the 800 °C treatment significantly enhancing the post-peak toughness behavior of the sample and reducing the differentiation of AE activity and energy release in four stages. In addition, we also observed the same trend in specimen W2-600. Although the temperature was less than 800 °C, the repeated α - β transformation and thermal shock during the five heating and water quenching cycles resulted in the enhancement of the density of internal defects such as microcracks and pores.

Mechanism of cracking induced by high temperature and water cooling

The effects of high temperature on the microstructure changes of sandstone mainly include water loss, thermal expansion cracking, and crystal phase transition (Yin et al. 2019). First, when the temperature is lower than 400 °C, the cohesive strength will not reduce significantly.

At this temperature, the mineral particles are heated and expand to squeeze the micro pores and microcracks inside the rock, causing the interlocking between micro-defects

faces (Sirdesai et al. 2017). In 25–400 °C, thermal cracks may also initiate with the growth of temperature, but due to the loose internal structure of sandstone, compaction takes the leading role in general. Sandstone specimens lose their moisture with the loss of free water and bound water at $T \leq 100$ °C and $T \leq 300$ °C, respectively (Zhang et al. 2017). The vaporization of free water and loosely bound water together with defects closure improve the contact of pore and crack surfaces, which is beneficial to enhancing strength and resistance to deformation. The interlocking between the thermal-induced microcrack faces is reflected not only in the porosity decrease (Fig. 4), but also in the pore structure. It can be seen from Fig. 12a that the curve in the corresponding range of nanopore and macropore of A1-400 is below A1-200, which means the closure of nanopore and macropore. This thermal-induced enhancement results in greater compressive and tensile resistance of the A1-400 than the A1-200. The pores in which lost water are filled with air, and the speed of ultrasonic waves in water is higher than in air. Therefore, variation in mechanical properties and P-wave velocity of A1 in 200 °C ~ 400 °C is inconsistent.

Moreover, when the temperature rises to 400~500 °C, the crystal water and water in the mineral structure will further escape from the rock, degrading cementation and mineral lattice skeleton (Zhang et al. 2016). Thermal crack initiation, propagation, and coalescence continue. Finally, as shown in Fig. 20a, the phase α transforms to β when $T \geq 573$ °C (Glover et al. 1995; Sun et al. 2013), during which the sudden increase in the volume of quartz causes existing crack propagation and new crack initiation inside the rock (Ohno 1995). The cracking behavior is irreversible, although the phase transition can be restored after cooling. This corresponds to the rapid decrease of mechanical strength and wave velocity and the deterioration of pore structure in A1 samples from 400 to 600 °C. In the range of 600~800 °C, the partial melting of minerals and cementing material occurred, and the further increase in heat generated thermal micro-cracks within the sub-grains contributed to the steady evolution in ultrasonic characteristics, porous structure, and mechanical property.

The effects of cooling medium and cooling rate on sandstone can be summarized as water weakening and thermal shock. On the one hand, when sandstone cools down in the water, infiltration of the moisture facilitates mineral recrystallization, while the free water weakens the connections between the mineral particles, resulting in more micro defects in the microstructure (Liu et al. 2017). On the other hand, compared with air-to-rock thermal conduction, water-to-rock thermal conduction is associated with higher cooling rates or quicker and greater temperature drops (Kumari et al. 2017). The rock is in a state of unsteady heat conduction during quenching, which results in uneven temperature distribution (Jin et al. 2019). As shown in Fig. 20b, a thermal stress field that distributes tensile stress on the outside and compressive stress in the inner part of specimen is formed at cooling (Collin and Rowcliffe 2002). The temperature stress induced by water cooling intensifies the stress concentration

at the tip of the existing thermal crack and leads to further crack development (Fellner and Supancic 2002). The effect of temperature gradient formed by thermal shock on the physical–mechanical properties of rock is much more significant than that of thermal expansion cracking (Sarici 2016). Therefore, the microcracks propagation induced by thermal shock tensile stress is the primary reason for the deterioration in rock properties under water cooling (Fan et al. 2020; Li et al. 2019; Yu et al. 2020). Numerous defects of W1 samples resulted in higher porosity, higher mesopore and macropore proportion, lower V_p , and more severely impaired integrity and compactness than air-cooled specimens. It should be pointed out that the thermal damage of water-cooled samples is caused by multiple factors during the two stages of heating and cooling. The degradation of the rock matrix by thermal shock precedes that by thermal-induced enhancement caused by mineral expansion and water evaporation. Herein, the monotonically decreasing of water-cooled samples (W1) is different from the first rise and then a descent of air-cooled samples (A1) at 200–800 °C.

Mechanism of damage by periodic heating and cooling treatments

The mechanism of the periodic action leading to differential damage can be explained as follows. Microcrack density is the main factor affecting the physical–mechanical properties of sandstone, which depends on the microcrack and pore evolution. At 200 °C, The multiscale pore of the periodic heating samples showed a closure tendency due to the improved contact of crack surface caused by mineral thermal expansion and water loss. The crack closure cancels the deterioration caused by thermal fatigue and thermal shock. At 400~600 °C, in the case of periodic heating–cooling, the alternating stress caused by the unmatched expansion and contraction of minerals causes microcrack and pore initiation in more positions

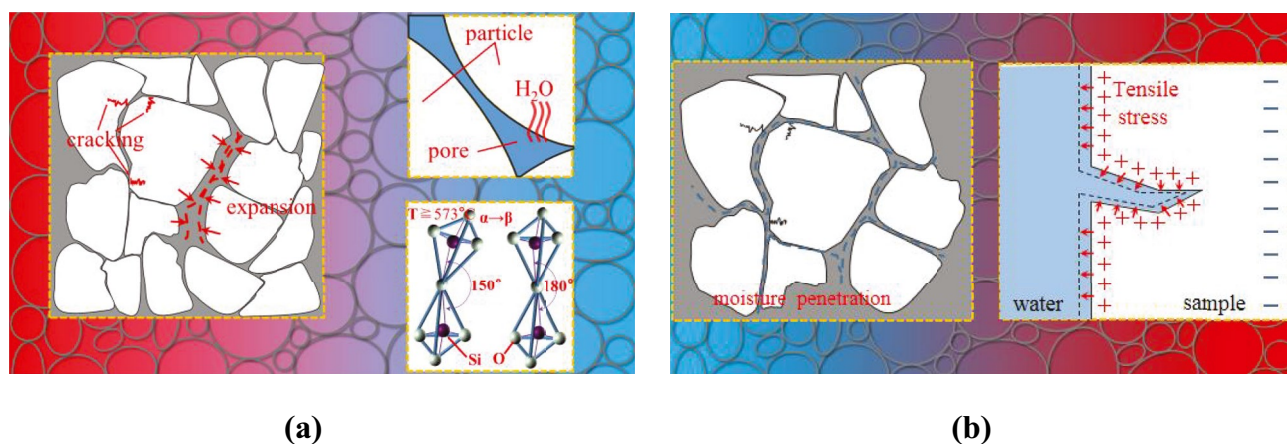


Fig. 20 Microscopic mechanism of a thermal cracking and b cooling effect of sandstone

inside the rock. The pore porosity of periodic thermal treated samples is generally more extensive than that of continuously heated ones (Figs. 13 and 14). Further observation of the increase in peak area (Fig. 13) shows that the rise in the peak area of the water-cooled nanopore (AW2–AW1) is smaller than that of the air-cooled nanopore (AA2–AA1). This means periodic water cooling will produce more microcracks than periodic air cooling, stimulating a dynamic transition from nanopore to micropore, mesopore, macropore, and even macroscopic fracture. Moreover, the stress at the crack tip is concentrated, and the peripheral constraints are reduced, making the gap develop continuously. The evolution of the gap provides a dominant path for the cooling medium, which makes the thermal shock continuously penetrate deep into the specimen. Therefore, more mesopores and macropores are formed in W2-600, resulting in a decrease in the number of nanopores rather than an increase, which can be seen intuitively in Fig. 18. With the repetition of heating–cooling, pores and microcracks continue to initiate, propagate, and coalesce. More large-scale cracks significantly reduce the strength, deformation resistance, and brittleness of the sandstone. The periodic heating and water cooling induced abundant microcracks and other defects inside the rock, which release part of the energy and result in a brittle to ductile transition. When sandstone is cooled at extremely high temperatures (800 °C), abundant micro-cracks excited by thermal fatigue significantly promote the connection and penetration of defects such as hot-melt holes and cracks, resulting in a sharp increase in the defect density and scale. The initiation of new microcracks, accompanied by the expansion and merging of various pores and cracks, reduces the pore structure uniformity and increases the uniformity coefficient to 44 (A2-800) and 53 (W2-800), as seen in Fig. 16. Intensive damage induced by the highest microcracking density that releases most of the energy leads to the degeneration of structure inside the rock, eventually leading to ductile characteristics in mechanical behavior presented in Figs. 6d and 8d (Wang et al. 2022a).

Conclusion

This paper studies the effects and damage mechanism of thermal fatigue caused by periodic heating–cooling on the dynamic evolution in porous structure and the mechanical behavior of sandstone. The following conclusions are drawn:

1. The sample treated by multiple thermal cycles at a lower temperature will also show thermal enhancement. A2-200 and W2-200 specimens show a higher UCS than the continuously heated specimens after five thermal cycles. On the contrary, the UCS of periodical heating specimens is lower than that of the continuously heating ones at 400, 600, and 800 °C. It can be concluded that crack closure caused by mineral thermal expansion and water loss counteracts the weakening effect in strength caused by thermal fatigue and thermal shock at 200 °C. However, the splitting test observes no noticeable tensile strength enhancement under the same thermal treatment conditions.
2. The BTS and UCS initially increase and then decrease with temperature for the continuously heating specimens, and the properties of periodical heating–cooling specimens strictly decrease. Repeated treatment at 200 °C enhances the brittleness of sandstone, while the brittle-ductility and failure mode transition are observed in periodic heating specimens at high temperatures.
3. AE monitoring captures the difference in AE ringing distribution among sandstones and quantitatively characterizes the mechanical damage evolution during failure process through AE events activity at each loading stage. The AE behavior confirmed that periodic heating promoted more cracking in the rock than continuous heat treatment within the same heating time.
4. The periodic heat treatment induced more nanopores than the continuous heating samples, but the proportion of nanopores in the total pores is also affected by pore propagation and coalescence. At 400 °C, compared with A1 and W1, the increased pores of A2 and W2 are mainly nanopores and micropores. At 600 °C, the nanopores and micropores of W2 are largely transformed into mesopores and macropores, while the increased pores of A2 remain in nanopores and micropores compared with A1. At 800 °C, the periodic heating and water cooling sample (W2) resulted in a significant increase in four types of pores, especially the nanopore and macropore, compared with W1. However, the mesopore and macropore of A2 have no significant increase compared with those of A1. Thermal fatigue leads to the porous structure evolution from uniformity to heterogeneity and increases the uniformity coefficient of pores.

Funding This research was supported by National Natural Science Foundation of China (No. 52004072, No. 52064006, and No. 52164001), the Guizhou Provincial Science and Technology Foundation (No. [2020]4Y044, No. [2021]292, No. [2020]2004, [2021]N404, and No. GCC[2022]005–1), the Youth Science and technology Talents Development Project of Guizhou Ordinary colleges and universities (No. [2022]140), the Research Fund for Talents of Guizhou University (Grant No. 201901), the Specialized Research Funds of Guizhou University (Grant No. 201903), and the Guangxi Zhuang Autonomous Region Science and Technology Foundation (No. 2020GXNSFAA159045).

Declarations

Conflict of interest The authors declare no competing interests.

References

- Bi J, Tang JC, Wang CL, Quan DG, Teng MY (2022) Crack coalescence behavior of rock-like specimens containing two circular embedded flaws. *Lithosphere* (special 11): 9498148. <https://doi.org/10.2113/1970/9498148>
- Bi J, Liu PF, Gan F (2020) Effects of the cooling treatment on the dynamic behavior of ordinary concrete exposed to high temperatures. *Constr Build Mater* 248. <https://doi.org/10.1016/j.conbuildmat.2020.118688>
- Breede K, Dzebisashvili K, Liu X, Falcone G (2013) A systematic review of enhanced (or engineered) geothermal systems: past, present and future. *Geotherm Energy* 1. <https://doi.org/10.1186/2195-9706-1-4>
- Brotóns V, Tomás R, Ivorra S, Alarcón JC (2013) Temperature influence on the physical and mechanical properties of a porous rock: San Julian's calcarenite. *Eng Geol* 167:117–127. <https://doi.org/10.1016/j.enggeo.2013.10.012>
- Caulk RA, Ghazanfari E, Perdrial JN, Perdrial N (2016) Experimental investigation of fracture aperture and permeability change within enhanced geothermal systems. *Geothermics* 62:12–21. <https://doi.org/10.1016/j.geothermics.2016.02.003>
- Chen YL, Ni J, Shao W, Azzam R (2012) Experimental study on the influence of temperature on the mechanical properties of granite under uni-axial compression and fatigue loading. *Int J Rock Mech Min Sci* 56:62–66. <https://doi.org/10.1016/j.ijrmms.2012.07.026>
- Collin M, Rowcliffe D (2002) The morphology of thermal cracks in brittle materials. *J Eur Ceram Soc* 22:435–445. [https://doi.org/10.1016/s0955-2219\(01\)00319-3](https://doi.org/10.1016/s0955-2219(01)00319-3)
- Eberhardt E, Stead D, Stimpson B, Read RS (1998) Identifying crack initiation and propagation thresholds in brittle rock. *Can Geotech J* 35:222–233. <https://doi.org/10.1139/t97-091>
- Fan LF, Gao JW, Du XL, Wu ZJ (2020) Spatial gradient distributions of thermal shock-induced damage to granite. *J Rock Mech Geotech* 12:917–926. <https://doi.org/10.1016/j.jrmge.2020.05.004>
- Fellner M, Supancic P (2002) Thermal shock failure of brittle materials. *Key Eng Mater* 223:97–106. <https://doi.org/10.4028/www.scientific.net/KEM.223.97>
- Ferreira APG, Farage MCR, Barbosa FS, Noumowé A, Renault N (2014) Thermo-hydric analysis of concrete–rock bilayers under fire conditions. *Eng Struct* 59:765–775. <https://doi.org/10.1016/j.engstruct.2013.11.033>
- Fleuchaus P, Godschalk B, Stober I, Blum P (2018) Worldwide application of aquifer thermal energy storage – a review. *Renew Sust Energy Rev* 94:861–876. <https://doi.org/10.1016/j.rser.2018.06.057>
- Fredrich JT, Wong T-f (1986) Micromechanics of thermally induced cracking in three crustal rocks. *J Geophys Res Solid Earth* 91:12743–12764. <https://doi.org/10.1029/JB091iB12p12743>
- Glover PWJ et al. (1995) α/β phase transition in quartz monitored using acoustic emissions. *120:775–782*. <https://doi.org/10.1111/j.1365-246X.1995.tb01852.x>
- Grant MA (2016) Physical Performance Indicators for HDR/EGS Projects. *Geothermics* 63:2–4. <https://doi.org/10.1016/j.geothermics.2015.01.004>
- Griffiths L, Lengline O, Heap MJ, Baud P, Schmittbuhl J (2018) Thermal cracking in westerly granite monitored using direct wave velocity, coda wave interferometry, and acoustic emissions. *J Geophys Res-Sol Ea* 123:2246–2261. <https://doi.org/10.1002/2017jb015191>
- Griffiths L, Heap MJ, Baud P, Schmittbuhl J (2017) Quantification of microcrack characteristics and implications for stiffness and strength of granite. *Int J Rock Mech Min Sci* 100:138–150. <https://doi.org/10.1016/j.ijrmms.2017.10.013>
- Guo QZ, Su HJ, Liu JW, Yin Q, Jing HW, Yu LY (2020) An experimental study on the fracture behaviors of marble specimens subjected to high temperature treatment. *Eng Fract Mech* 225:12. <https://doi.org/10.1016/j.engfracmech.2019.106862>
- Hähnlein S, Bayer P, Ferguson G, Blum P (2013) Sustainability and policy for the thermal use of shallow geothermal energy. *Energy Policy* 59:914–925. <https://doi.org/10.1016/j.enpol.2013.04.040>
- Han GS, Jing HW, Su HJ, Liu RC, Yin Q, Wu JY (2019) Effects of thermal shock due to rapid cooling on the mechanical properties of sandstone. *Environ Earth Sci* 78. <https://doi.org/10.1007/s12665-019-8151-1>
- Hao J, Qiao L, Liu Z, Li Q (2022) Effect of thermal treatment on physical and mechanical properties of sandstone for thermal energy storage: a comprehensive experimental study. *Acta Geotech* 17:3887–3908. <https://doi.org/10.1007/s11440-022-01514-8>
- Heiple CR, Carpenter SH (1983) Acoustic emission from dislocation motion. Gordon and Breach Science Publishers, New York
- Heuze FE (1983) High-temperature mechanical, physical and thermal properties of granitic rocks—a review. *Int J Rock Mech Min Sci Geomech Abstr* 20:3–10. [https://doi.org/10.1016/0148-9062\(83\)91609-1](https://doi.org/10.1016/0148-9062(83)91609-1)
- Hodot B (1966) Outburst of coal and coalbed gas (Chinese translation). China Coal Industry Press, Beijing
- Huang Z, Zeng W, Wu Y, Li S, Gu Q, Zhao K (2021) Effects of temperature and acid solution on the physical and tensile mechanical properties of red sandstones. *Environ Sci Pollut Res Int* 28:20608–20623. <https://doi.org/10.1007/s11356-020-11866-x>
- Isaka BLA, Gamage RP, Rathnaweera TD, Perera MSA, Chandrasekharam D, Kumari WGP (2018) An influence of thermally-induced micro-cracking under cooling treatments: mechanical characteristics of australian granite. *Energies* 11:24. <https://doi.org/10.3390/en11061338>
- Jia H, Ding S, Zi F, Dong Y, Shen Y (2020) Evolution in sandstone pore structures with freeze-thaw cycling and interpretation of damage mechanisms in saturated porous rocks. *Catena* 195. <https://doi.org/10.1016/j.catena.2020.104915>
- Jin PH, Hu YQ, Shao JX, Zhao GK, Zhu XZ, Li C (2019) Influence of different thermal cycling treatments on the physical, mechanical and transport properties of granite. *Geothermics* 78:118–128. <https://doi.org/10.1016/j.geothermics.2018.12.008>
- Kim K, Kemeny J, Nickerson M (2014) Effect of rapid thermal cooling on mechanical rock properties. *Rock Mech Rock Eng* 47:2005–2019. <https://doi.org/10.1007/s00603-013-0523-3>
- Kompanikova Z, Gomez-Heras M, Michnova J, Durmekova T, Vlcko J (2014) Sandstone alterations triggered by fire-related temperatures. *Environ. Earth Sci* 72:2569–2581. <https://doi.org/10.1007/s12665-014-3164-2>
- Kumari WGP, Ranjith PG, Perera MBA, Chen BK, Abdulagatov IM (2017) Temperature-dependent mechanical behaviour of Australian Strathbogie granite with different cooling treatments. *Eng Geol* 229:31–44. <https://doi.org/10.1016/j.enggeo.2017.09.012>
- Laouafa F, Farret R, Vidal-Gilbert S, Kazmierczak JB (2016) Overview and modeling of mechanical and thermomechanical impact of underground coal gasification exploitation. *Mitig Adapt Strat Gl* 21:547–576. <https://doi.org/10.1007/s11027-014-9542-y>
- Li Q, Yin T, Li X, Zhang S (2019) Effects of rapid cooling treatment on heated sandstone: a comparison between water and liquid nitrogen cooling. *B Eng Geol Environ* 79:313–327. <https://doi.org/10.1007/s10064-019-01571-6>
- Liu Q, Qian Z, Wu Z (2017) Micro/macro physical and mechanical variation of red sandstone subjected to cyclic heating and cooling: an experimental study. *B Eng Geol Environ* 78:1485–1499. <https://doi.org/10.1007/s10064-017-1196-z>
- Liu BX, Huang JL, Wang ZY, Liu L (2009) Study on damage evolution and acoustic emission character of coal-rock under uniaxial compression. *Chin J Rock Mech Eng* 28:3234–3238. <https://doi.org/10.3321/j.issn:1000-6915.2009.z1.096>
- Martin CD, Chandler NA (1994) The progressive fracture of Lac du Bonnet granite. *Int J Rock Mech Min Sci Geomech Abstr* 31:643–659. [https://doi.org/10.1016/0148-9062\(94\)90005-1](https://doi.org/10.1016/0148-9062(94)90005-1)

- Matteson A, Tomanic JP, Herron MM, Allen DF, Kenyon WE (2000) NMR relaxation of clay/brine mixtures. *SPE Reserv Eval Eng* 3:602–603. <https://doi.org/10.2118/49008-MS>
- Meredith PG, Main IG, Clint OC, Li L (2012) On the threshold of flow in a tight natural rock. *GeoRL* 39:5. <https://doi.org/10.1029/2011gl050649>
- Miao S, Pan P-Z, Yu P, Zhao S, Shao C (2020) Fracture analysis of Beishan granite after high-temperature treatment using digital image correlation. *Eng Fract Mech* 225:106847. <https://doi.org/10.1016/j.engfracmech.2019.106847>
- Niu SW, Zhao YS, Hu YQ (2014) Experimental investigation of the temperature and pore pressure effect on permeability of lignite under the in situ condition. *Transport Porous Med* 101:137–148. <https://doi.org/10.1007/s11242-013-0236-9>
- Ohno I (1995) Temperature variation of elastic properties of ALPHA.-Quartz up to the ALPHA.-BETA. transition. *JPE* 43:157–169. <https://doi.org/10.4294/jpe1952.43.157>
- Pathiranagei SV, Gratchev I (2021) Engineering properties of sandstone heated to a range of high temperatures. *B Eng Geol Environ* 80:2415–2432. <https://doi.org/10.1007/s10064-020-02065-6>
- Ranjith PG, Viete DR, Chen BJ, Perera MSA (2012) Transformation plasticity and the effect of temperature on the mechanical behaviour of Hawkesbury sandstone at atmospheric pressure. *Eng Geol* 151:120–127. <https://doi.org/10.1016/j.enggeo.2012.09.007>
- Rawal C, Ghassemi A (2014) A reactive thermo-poroelastic analysis of water injection into an enhanced geothermal reservoir. *Geothermics* 50:10–23. <https://doi.org/10.1016/j.geothermics.2013.05.007>
- Richter D, Simmons G (1974) Thermal expansion behavior of igneous rocks. *Int J Rock Mech Min Sci Geomech Abstr* 11:403–411. [https://doi.org/10.1016/0148-9062\(74\)91111-5](https://doi.org/10.1016/0148-9062(74)91111-5)
- Sarici DE (2016) Thermal deterioration of marbles: gloss, color changes. *Constr Build Mater* 102:416–421. <https://doi.org/10.1016/j.conbuildmat.2015.10.200>
- Sha S, Rong G, Chen ZH, Li BW, Zhang ZY (2020) Experimental evaluation of physical and mechanical properties of geothermal reservoir rock after different cooling treatments. *Rock Mech Rock Eng* 53:4967–4991. <https://doi.org/10.1007/s00603-020-02200-5>
- Shao SS, Ranjith PG, Wasantha PLP, Chen BK (2015) Experimental and numerical studies on the mechanical behaviour of Australian Strathbogie granite at high temperatures: an application to geothermal energy. *Geothermics* 54:96–108. <https://doi.org/10.1016/j.geothermics.2014.11.005>
- Siratovich PA, Villeneuve MC, Cole JW, Kennedy BM, Begue F (2015) Saturated heating and quenching of three crustal rocks and implications for thermal stimulation of permeability in geothermal reservoirs. *Int J Rock Mech Min Sci* 80:265–280. <https://doi.org/10.1016/j.ijrmms.2015.09.023>
- Sirdesai NN, Singh TN, Gamage RP (2017) Thermal alterations in the poromechanical characteristic of an Indian sandstone – a comparative study. *Eng Geol* 226:208–220. <https://doi.org/10.1016/j.enggeo.2017.06.010>
- Sirdesai NN, Singh TN, Ranjith PG, Singh R (2016) Effect of varied durations of thermal treatment on the tensile strength of red sandstone. *Rock Mech Rock Eng* 50:205–213. <https://doi.org/10.1007/s00603-016-1047-4>
- Smith AG, Pells PJN (2008) Impact of fire on tunnels in Hawkesbury sandstone. *Tunn Undergr Sp Tech* 23:65–74. <https://doi.org/10.1016/j.tust.2006.11.003>
- Sun H, Sun Q, Deng WN, Zhang WQ, Lu C (2017a) Temperature effect on microstructure and P-wave propagation in Linyi sandstone. *Appl Therm Eng* 115:913–922. <https://doi.org/10.1016/j.applthermaleng.2017.01.026>
- Sun Q, Zhang Z, Xue L, Zhu S (2013) Physico-mechanical properties variation of rock with phase transformation under high temperature. *Chin J Rock Mech Eng*. <https://doi.org/10.3969/j.issn.1000-6915.2013.05.011>
- Sun ZX et al (2017b) Numerical simulation of the heat extraction in EGS with thermal-hydraulic-mechanical coupling method based on discrete fractures model. *Energy* 120:20–33. <https://doi.org/10.1016/j.energy.2016.10.046>
- Tang CA, Chen ZH, Xu XH, Li C (1997) A theoretical model for kaiser effect in rock. *Pure Appl Geophys* 150:203–215. <https://doi.org/10.1007/s000240050073>
- Wadley HNG, Scruby CB, Speake JH (2013) Acoustic emission for physical examination of metals. *IMErv* 25:41–64. <https://doi.org/10.1179/imtr.1980.25.1.41>
- Wang CL, Zhao Y, He C, Bi J (2022a) Study on the tensile-shear mechanical behavior of sandstone using a simple auxiliary apparatus. *Theor Appl Fract Mec* 122:103608. <https://doi.org/10.1016/j.tafmec.2022.103608>
- Wang CL, Zhao Y, Ning L, Bi J (2022b) Permeability evolution of coal subjected to triaxial compression based on in-situ nuclear magnetic resonance. *Int J Rock Mech Min Sci* 159. <https://doi.org/10.1016/j.ijrmms.2022.105213>
- Wichtmann T, Triantafyllidis T (2013) Effect of uniformity coefficient on g/gmax and damping ratio of uniform to well-graded quartz sands. *J Geotech Geoenviron Eng* 139:59–72. [https://doi.org/10.1061/\(asce\)gt.1943-5606.0000735](https://doi.org/10.1061/(asce)gt.1943-5606.0000735)
- Xie K, Jiang D, Sun Z, Chen J, Zhang W, Jiang X (2018) NMR, MRI and AE statistical study of damage due to a low number of wetting–drying cycles in sandstone from the three gorges reservoir area. *Rock Mech Rock Eng* 51:3625–3634. <https://doi.org/10.1007/s00603-018-1562-6>
- Yang SQ, Xu P, Li YB, Huang YH (2017) Experimental investigation on triaxial mechanical and permeability behavior of sandstone after exposure to different high temperature treatments. *Geothermics* 69:93–109. <https://doi.org/10.1016/j.geothermics.2017.04.009>
- Yavuz H, Demirdag S, Caran S (2010) Thermal effect on the physical properties of carbonate rocks. *Int J Rock Mech Min Sci* 47:94–103. <https://doi.org/10.1016/j.ijrmms.2009.09.014>
- Yin TB, Li Q, Li XB (2019) Experimental investigation on mode I fracture characteristics of granite after cyclic heating and cooling treatments. *Eng Fract Mech* 222. <https://doi.org/10.1016/j.engfracmech.2019.106740>
- Yu PY, Pan PZ, Feng GL, Wu ZH, Zhao SK (2020) Physico-mechanical properties of granite after cyclic thermal shock. *J Rock Mech Geotech* 12:693–706. <https://doi.org/10.1016/j.jrmge.2020.03.001>
- Zhang WQ, Sun Q, Hao SQ, Geng JS, Lv C (2016) Experimental study on the variation of physical and mechanical properties of rock after high temperature treatment. *Appl Therm Eng* 98:1297–1304. <https://doi.org/10.1016/j.applthermaleng.2016.01.010>
- Zhang YL, Sun Q, He H, Cao LW, Zhang WQ, Wang B (2017) Pore characteristics and mechanical properties of sandstone under the influence of temperature. *Appl Therm Eng* 113:537–543. <https://doi.org/10.1016/j.applthermaleng.2016.11.061>
- Zhao Y, Wang CL, Ning L, Zhao HF, Bi J (2022a) Pore and fracture development in coal under stress conditions based on nuclear magnetic resonance and fractal theory. *Fuel* 309:122112. <https://doi.org/10.1016/j.fuel.2021.122112>
- Zhao Y, Zheng K, Wang C, Bi J, Zhang H (2022b) Investigation on model-I fracture toughness of sandstone with the structure of typical bedding inclination angles subjected to three-point bending. *Theor Appl Fract Mec* 119. <https://doi.org/10.1016/j.tafmec.2022.103327>
- Zhu D, Jing HW, Yin Q, Han GS (2018) Experimental study on the damage of granite by acoustic emission after cyclic heating and cooling with circulating water. *Processes* 6. <https://doi.org/10.3390/pr6080101>

Springer Nature or its licensor (e.g. a society or other partner) holds exclusive rights to this article under a publishing agreement with the author(s) or other rightsholder(s); author self-archiving of the accepted manuscript version of this article is solely governed by the terms of such publishing agreement and applicable law.